Russian Chemical Reviews **75** (1) 77 – 93 (2006) © 2006 Russian Academy of Sciences and Turpion Ltd

DOI 10.1070/RC2006v075n01ABEH003596

Magnetic properties of bismuth(III) oxy compounds

E A Kravchenko, V G Orlov, M P Shlykov

Contents

I.	Introduction	77
II.	Splitting of the ^{209}Bi NQR spectra of bismuth(III) oxy compounds in internal magnetic fields	78
III.	^{209}Bi NQR experiments on $Bi_4Ge_3O_{12}$ and $Bi_3B_5O_{12}$ single crystals in external magnetic fields	79
IV.	Studies of local magnetic fields by analysis of the quadrupole spin echo envelope	83
V.	The results of magnetisation measurements and magnetoelectric effect in the α-Bi_2O_3 single crystal	86
VI.	On the probable origin of anomalies in magnetic properties of bismuth oxy compounds	89
VII.	Conclusion	90
VIII.	Appendix. The calculation of the nuclear quadrupole spin echo	90

Abstract. Nuclear quadrupole resonance and SQUID-magnetometric studies on magnetic properties of bismuth(III) oxy compounds comprising neither d- nor f-elements are surveyed and systematised. The magnetic properties, not conventionally expected in the Main Group element substances, were found to exist in most of the compounds discussed. The results of the analysis of the zero-field ^{209}Bi NQR line shapes, the Zeeman-perturbed patterns in external fields of various orientations with respect to the crystal axes, and the spin-echo envelopes suggest the existence in α-Bi_2O_3, Bi_3O_4Br, $Bi_2Al_4O_9$, $Bi_2Ge_3O_9$, $Bi_4Ge_3O_{12}$ and $BaBiO_2Cl$, of ordered magnetic fields ranging from 30 to 250 G, which notably exceed the dipole nuclear magnetic fields. The magnetoelectric effect was observed in the α-Bi_2O_3 single crystal, and the paramagnetism depending on the thermal prehistory of the crystal was found using a SQUID-technique. The questions concerning the origin of unusual magnetic and electronic properties of the title compounds are discussed. The bibliography includes 49 references.

I. Introduction

Bismuth oxide α-Bi_2O_3 and related compounds are parent substances for the preparation of high-temperature superconductors and ferroelectrics, and some of them are materials exhibiting valuable electroacoustic, piezoelectric and nonlinear optical properties. However, in spite of the interest of researchers, the magnetic properties of these compounds have not been explored adequately. The ^{209}Bi nuclear quadrupole resonance (NQR) spectra suggest that α-Bi_2O_3, Bi_3O_4Br, $Bi_2Al_4O_9$, $Bi_2Ge_3O_9$, $Bi_4Ge_3O_{12}$, $BaBiO_2Cl$ and $Bi_3B_5O_{12}$ comprising no magnetism carriers, *i.e.*, atoms of d- or f-elements, are not diamagnets in the conventional sense. Local ordered magnetic fields (H_{loc}) up to 250 G in these compounds cause, in some of them, typical Zeeman splittings of the ^{209}Bi NQR lines in the absence of external magnetic fields (see Refs 1 – 4 and references cited therein). Their NQR spectra reveal an extraordinarily high sensitivity of the electronic characteristics to weak (H_e < 500 Œ) external magnetic fields, which suggests a strong coupling between the magnetic and electronic subsystems of the substances. This, in principle, points to a possibility of governing the functional properties of the corresponding materials by applying weak magnetic fields. For instance, a dramatic increase in the line intensity was observed in the ^{209}Bi NQR spectrum of $Bi_4Ge_3O_{12}$ upon applying an external magnetic field, which is not described within the conventional theory of the Zeeman NQR spectroscopy.

The NQR spectroscopy is recognised as a direct, most efficient and precise method of detecting and studying the nuclear quadrupole interactions, because the quadrupolar Hamiltonian is determined by interactions between the nuclear electric quadrupole moment Q (all the nuclei with spin $I > 1/2$ have such a moment) and the electric field gradient (EFG)

$$q_{ij} = \frac{\partial E_i}{\partial j} = -\frac{\partial^2 U}{\partial ij},$$

where E is the strength of the electrostatic field, U is the electrostatic potential at the nuclear site and $i, j = x, y, z$. The quadrupole coupling constant

$$QCC = \frac{eQq_{zz}}{h}$$

and the EFG asymmetry parameter

$$\eta = \frac{q_{xx} - q_{yy}}{q_{zz}}$$

are the parameters that are measured.

Their values are directly related to the electron density distribution around the nucleus studied. As a result, any weak disturbance of the electron density is clearly and adequately reflected in the NQR spectra. The NQR spectroscopy may be used for studies of a wide variety of phenomena accompanied by changes in the electric fields in the vicinity of the resonance nuclei, and NQR was used as the basic method of investigating the problems discussed. The physical principles of the NQR phenom-

E A Kravchenko N S Kurnakov Institute of General and Inorganic Chemistry, Russian Academy of Sciences, Leninsky prosp. 31, 119991 Moscow, Russian Federation. Fax (7-495) 954 12 79, tel. (7-495) 955 48 22, e-mail: ekravchenko@igic.ras.ru
V G Orlov, M P Shlykov Russian Research Centre 'Kurchatov Institute', pl. Kurchatova 1, 123182 Moscow, Russian Federation. Fax (7-495) 196 18 70, tel. (7-495) 196 95 19, e-mail: orlov@mbslab.kiae.ru (V G Orlov), shlykov@mbslab.kiae.ru (M P Shlykov)

Received 5 August 2005
Uspekhi Khimii **75** (1) 86 – 104 (2006); translated by E A Kravchenko

enon, the scope and limitations of NQR spectroscopy in application to problems of inorganic chemistry have been reviewed.[5,6]

The results of investigations showed that the methods based on measurement of nuclear quadrupole interactions are highly sensitive to the presence of a magnetic field in a substance. The experiments discussed in the present review involved studies of the zero-field ^{209}Bi NQR line shapes in crystalline powders and single crystals, analysis of splittings in the spectra of single crystals in external magnetic fields (H_e) of various orientations with respect to the crystal axes (the Zeeman experiment) and examination of the shapes of the quadrupole spin-echo envelopes (SEE). The experiments recording the SEE in the spectra of crystalline powders enable one to detect small (within the line width) splittings observed as modulations of the SEE curves. Subsequent mathematical processing and computer simulation of either the Zeeman splittings or the SEE shape give the quantitative characteristics of the internal source of splittings, namely, the strength and orientation of the local magnetic field.

The ^{209}Bi NQR Zeeman spectra of the majority of compounds discussed in this review displayed multiplicities, which points to the magnetic non-equivalence of bismuth positions. Therefore, the computer simulation required analysis of the symmetry properties of the EFG tensor. This analysis was based on the crystal-field potential model developed by Orlov.[7]

II. Splitting of the ^{209}Bi NQR spectra of bismuth(III) oxy compounds in internal magnetic fields

The zero-field ^{209}Bi NQR spectrum (the ^{209}Bi nuclear spin is 9/2) comprises a set of four transitions between five doubly degenerate energy levels $|\pm m\rangle$; their frequencies, assuming the simplest case of magnetic equivalence of the bismuth sites and $\eta = 0$, are determined as

$$\nu_k = \frac{3keQq_{zz}}{2I(2I-1)h},$$

where $k = 1, ..., 4$.

Figure 1 shows the diagram of the ^{209}Bi NQR spectra of a single crystal in zero and non-zero external magnetic field of arbitrary orientation with respect to the EFG axes. A perturbing static magnetic field H_e removes the double degeneracy $\pm m$ of the quadrupole energy levels, because the energy of interaction of the nuclear magnetic moment with this field becomes different for the orientations of the nuclear spin projection along and opposite the $\boldsymbol{H}_e$ direction. In this case, each singlet, assigned to the resonance transition $\pm m \rightarrow \pm (m+1)$, at $m > 1/2$ is split into a doublet with the separation between the components

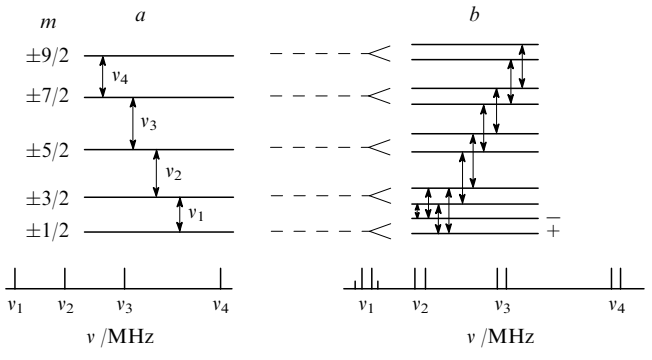


Figure 1. Diagrams of quadrupole energy levels and transitions between them for the ^{209}Bi nucleus (spin 9/2) in zero (*a*) and Zeeman (*b*) magnetic fields.

$$\Delta\nu = 2\gamma H_e\cos\theta, \tag{1}$$

where γ is the gyromagnetic ratio for the quadrupole nucleus and θ is the angle between the EFG q_{zz} axis and $\boldsymbol{H}_e$. The doublet components are symmetrical about the original non-split NQR frequency ν_n, and their total intensity is equal to that of the initial non-split line.[8] The lowest levels $m = \pm 1/2$ mix in external magnetic field to produce new states ψ_+ and ψ_- and hence a quadruplet, centred at the frequency of the unperturbed transition $\nu_{\pm 1/2} \rightarrow \nu_{\pm 3/2}$

$$\nu_\alpha = \frac{6A}{h} - \frac{1}{2}(3-f)\gamma H_e\cos\theta, \tag{2}$$

$$\nu_\beta = \frac{6A}{h} - \frac{1}{2}(3+f)\gamma H_e\cos\theta,$$

$$\nu_\alpha' = \frac{6A}{h} + \frac{1}{2}(3-f)\gamma H_e\cos\theta,$$

$$\nu_\beta' = \frac{6A}{h} + \frac{1}{2}(3+f)\gamma H_e\cos\theta,$$

where

$$A = \frac{eQq_{zz}}{4I(2I-1)},$$

$$f = \left[1 + \left(I + \frac{1}{2}\right)^2 \tan^2\theta\right]^{1/2}.$$

The quadruplet components are also symmetrical about the frequency of the unperturbed transition.[8]

Thus, the presence in the spectrum of a quartet of lines assigned to the lowest transition ν_1 ($\Delta m = 1/2 - 3/2$) and doublets to the remaining transitions ($\nu_2, ..., \nu_n$) points to the magnetic nature of the splittings, hence excluding the crystallographic non-equivalence of atomic positions as the cause for the splittings. The separations between the doublet components $\nu_\alpha(\nu_\alpha')$ and $\nu_\beta(\nu_\beta')$ are evidently determined by equations

$$\Delta\nu_\alpha = (3-f)\gamma H_e\cos\theta, \tag{3}$$

$$\Delta\nu_\beta = (3+f)\gamma H_e\cos\theta.$$

which show that the number of components (multiplicity) and their frequencies depend on the strength and orientation of the Zeeman field H_e with respect to the EFG axes of a single crystal.

Figure 2 demonstrates the ^{209}Bi NQR line shapes recorded in zero applied field for α-Bi_2O_3 and Bi_3O_4Br. One can see that both

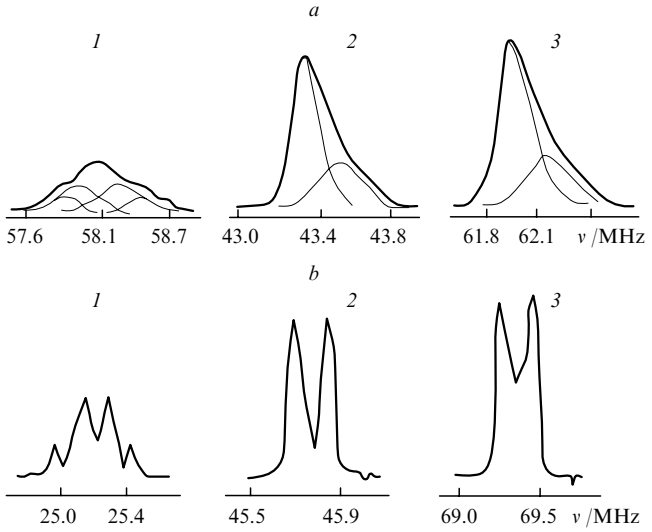


Figure 2. The ^{209}Bi NQR spectral lines assigned to the transitions ν_1 (*1*), ν_2 (*2*), ν_3 (*3*) (see Table 1) in Bi_3O_4Br (*a*) and α-Bi_2O_3 (*b*).

Table 1. The zero-field ^{209}Bi NQR spectra and values of H_{loc} in bismuth oxy compounds (the frequencies are averaged over splittings).[2,4]

Compound	T /K	Transition frequencies (MHz) $\nu_n = m_i \rightarrow m_{i+1}$				eQq/h /MHz	η (%)	H_{loc} /G
		ν_1	ν_2	ν_3	ν_4			
α-Bi_2O_3								
Bi(1)	77	25.2	45.8	69.4	92.8	556.7	0.13	171
Bi(2)		39.3	37.2	58.3	79.4	482.6	0.40	136
Bi_3O_4Br								
Bi(1)	77	21.6	25.1	39.6	53.3	322.6	0.31	–
Bi(2)		58.0	43.4	61.9	86.6	536.9	0.62	250 ± 10
$Bi_2Al_4O_9$	77	33.15	50.5	78.0	104.1	626.4	0.19	150 ± 10
$Bi_4Ge_3O_{12}$	300	20.4	40.9	61.3	81.7	490.3	0.0	25 ± 5
$Bi_2Ge_3O_9$	77	25.7	51.6	77.35	103.2	618.8	0.0	60 ± 10
	300	25.25	50.5	75.7	101.0	605.9	0.0	–

splitting patterns appear as typical Zeeman-perturbed NQR patterns for nuclei having spin $I > 3/2$: the lowest line ν_1 ($\Delta m = 1/2 - 3/2$) is split into a quadruplet, and the lines of higher frequency transitions ν_2, ν_3, into doublets. This evidences that an internal source of the line splittings exists in these compounds, namely, a local ordered magnetic field H_{loc}, which has a fixed orientation with respect to the nuclear spin direction. This is supported by the observation of the zero-field splittings not only in single crystals, but also in powders. Each crystallite in a powder sample is a single crystal for the local magnetic field, so the observation of the zero-field Zeeman splittings in powder samples rules out the suggestion that an impurity may be the cause for the splittings.

The zero-field splittings were later observed in the ^{209}Bi NQR spectra of several other bismuth oxy compounds, $Bi_2Al_4O_9$, $Bi_4Ge_3O_{12}$ and $Bi_2Ge_3O_9$,[3,4] although the X-ray data [9–11] show that the bismuth sites are crystallographically equivalent in their structures. This also excludes the crystallographic non-equivalence as the cause for the spectroscopic splittings. Analysis of the splittings showed that they are consistent with local ordered magnetic fields of 25–250 G notably exceeding the dipole nuclear magnetic fields (about several G). Therefore, the electronic system solely can be the source of the fields in the compounds in question. On the other hand, the values of H_{loc} are several orders of magnitude smaller than those in conventional ferro- and antiferromagnets, which is indicative of a new phenomenon. The ^{209}Bi NQR spectra of the compounds mentioned and the values of H_{loc} estimated from the zero-field splittings are listed in Table 1.

III. ^{209}Bi NQR experiments on $Bi_4Ge_3O_{12}$ and $Bi_3B_5O_{12}$ single crystals in external magnetic fields

Small values of splittings and low intensities of some of the transitions made difficult further studies of magnetic properties in the zero field. They were continued in weak external magnetic fields with a view to study the Zeeman splittings in the ^{209}Bi NQR spectra of single crystals. This approach appeared to be efficient because the Zeeman spectra of single crystals exhibited some specific features most clearly revealed on the change in the orientation of external magnetic fields with respect to the crystal axes. The single crystals of $Bi_4Ge_3O_{12}$ and $Bi_3B_5O_{12}$ were studied extensively.[12–15]

The Zeeman fields H_e from 0 to 500 Œ were applied either parallel or perpendicularly to the direction of the radiofrequency field ($\boldsymbol{H}_{rf}$). The crystals were turned in the rf-coil about the $\boldsymbol{H}_{rf}$ direction at a definite angle α, which changed the orientation of $\boldsymbol{H}_e$ with respect to the crystallographic axes of the samples. This procedure allowed detailed studies on the shapes, intensities and multiplicities of the resonance lines as functions of mutual orientation of the fields disturbing the bismuth nuclear magnetic moments. A pulse NQR spectrometer, which enabled continuous scanning through the frequency range required, was used for the experiments.

The $Bi_4Ge_3O_{12}$ single crystal had a shape of parallelepiped ($6 \times 9 \times 25$ mm) with a (100) crystallographic plane perpendicular to the radiofrequency coil axis that coincided with the $\boldsymbol{H}_{rf}$ direction. On successive variation of the strength and orientation of $\boldsymbol{H}_e$ during the experiment, the ^{209}Bi NQR lines of the $\nu_1 - \nu_3$ transitions were recorded at several positions of the crystal in the coil.[12]

If the spin system is simultaneously disturbed by both local and external magnetic fields, the Zeeman spectrum shown in Fig. 1 *b* is expected to become more complicated. As was mentioned above, this is chiefly determined by the crystal symmetry of the compound studied. The number of components (multiplicity), their frequencies and intensities depend also on the strength and orientation of the fields $\boldsymbol{H}_e$ and $\boldsymbol{H}_{loc}$. Therefore, a theoretical modelling that takes into account the crystal symmetry is necessary for the interpretation of the spectra.

The package of programs [12] for the modelling of the Zeeman splittings in the ^{209}Bi NQR spectra of single crystal included no approximate analytical expressions for the nuclear spin energy levels or transition probabilities. The calculation of these parameters by diagonalisation of the quadrupolar Hamiltonian was carried out numerically with any desired accuracy. After that, the evolution of the spectroscopic splittings was simulated for the given strength and orientation of $\boldsymbol{H}_e$ with respect to the crystal axes. By comparing the simulated and observed splittings, the strength of $\boldsymbol{H}_{loc}$ and angular parameters specifying the field orientation with respect to the EFG axes at the bismuth sites, were derived. The basic stages of the simulation of the ^{209}Bi NQR Zeeman spectra of the $Bi_4Ge_3O_{12}$ single crystal [12] are briefly described below and summarised in the Appendix.

According to X-ray diffraction data,[9,10] all the sixteen bismuth atoms in the unit cell of the eulitine-type structure (space group $I\bar{4}3d$), to which $Bi_4Ge_3O_{12}$ belongs, occupy the *c*-type sites in the threefold rotation axis. These positions are characterised by four magnetically non-equivalent EFG tensors. The direction of the maximum component $q_{z'z'}$ for each EFG tensor (x', y', z' are the EFG principal axes) with respect to the crystallographic system (x, y, z) is found by diagonalisation of the tensors. This direction is determined by the Euler angles θ and φ connecting the co-ordinate systems (x, y, z) and (x', y', z') (Fig. 3). The third Euler angle ψ, which specifies the direction of the axes x' and y' in the plane perpendicular to the z'-axis, remains arbitrary in consistence with the zero EFG asymmetry parameter at the bismuth sites in the eulitine structure. The angle ψ does not affect line splittings in the NQR spectra in a magnetic field, influencing only line intensity. With the symmetry properties of the lattice contribution to the EFG tensor taken into account, the relationship between the angular parameters of the principal axes $q_{z'z'}$ was derived for all the four EFG tensors:[12]

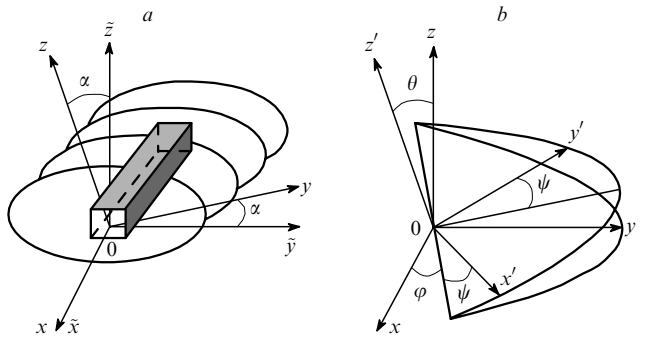


Figure 3. Mutual orientation of the Cartesian coordinate systems: the laboratory frame ($\tilde{x}$, $\tilde{y}$, $\tilde{z}$) and the system referred to the crystallographic axes (x,y, z) (*a*); the system referred to the crystallographic axes and to the EFG principal axes (x', y', z') (*b*).

$$\theta,\ \varphi;\ \ \pi-\theta,\ \varphi;\ \ \theta,\ \pi-\varphi;\ \ \pi-\theta,\ \pi-\varphi. \tag{4}$$

Hence, one has to find the angular parameters θ and φ for the principal axes of only one EFG tensor, those for three remaining ones being determined by the relationships (4).

In the absence of local and external magnetic fields and at $\eta = 0$, the energy of the nuclear spin levels E_j ($j = 1, 2, \ldots, 10$) and the appropriate eigenfunctions Y_j are calculated by diagonalisation of the simplest quadrupolar Hamiltonian:

$$\hat{H}_Q = \frac{eQq}{4I(2I-1)}\left[3I_{z'}^2 - I(I+1)\right], \tag{5}$$

where $eQq/h = 490.3$ MHz (see Table 1). The frequencies of transitions between the appropriate quadrupole levels are the same for all the four EFG tensors, because the Hamiltonian (5) does not depend on the parameters (4). In other words, in the absence of magnetic fields, all the bismuth sites in the eulitine structure are equivalent and the NQR spectra are indistinguishable. The observed singlets assigned to each of the four transitions ($k = 1, \ldots, 4$, see Fig. 1 *a*) represent superposition of four lines with identical frequencies and intensities. An external magnetic field directed at different angles to the four EFG principal axes systems makes the bismuth positions in the eulitine structure magnetically non-equivalent. In general, the NQR line can split into a maximum of 16 components (four quadruplets) for the transition $\Delta m = 1/2-3/2$ and 8 (4 doublets), for all the remaining transitions, the EFG symmetry properties (4) being taken into account. The angles θ and φ can be determined from the measured splittings of the Zeeman spectra of the oriented single crystal. The orientation of the laboratory system ($\tilde{x}$,$\tilde{y}$,$\tilde{z}$) is determined by the field directions as $\tilde{x} \,||\, \boldsymbol{H}_{\rm rf}$ and $\tilde{z} \,||\, \boldsymbol{H}_{\rm e}$ (see Fig. 3). Because the quadrupole Hamiltonian (5) was determined in the system of the EFG principal axes, a projection of vector $\boldsymbol{H}_{\rm e}$ onto the axes (x', y', z') is to be used in the Hamiltonian of interaction of the nuclear magnetic moment with external magnetic field $\hat{H}_{\rm e}$. This procedure is performed using a rotation matrix D, whose particular form is determined by orientation of the single crystal axes with respect to the laboratory system. Hence, the matrix D depends on the angle of sample turn in the rf-coil from the initial position ($\alpha = -45^\circ$) and from the Euler angles θ, φ and ψ. It is to be reminded that in the reported experiments,[12] the $Bi_4Ge_3O_{12}$ single crystal was placed in the rf-coil so that its longer axis [100] was parallel to the coil axis. The direction of $\boldsymbol{H}_{\rm e}$ in the initial position of the crystal was perpendicular to the plane $(0\bar{1}1)$.

If the spin system of a quadrupole nucleus is simultaneously disturbed by both local and external magnetic fields, the nuclear spin energy levels and their eigenfunctions are evaluated by diagonalisation of the Hamiltonian [12]

$$\hat{H} = \hat{H}_Q + \hat{H}_{\rm loc} + \hat{H}_{\rm e}, \tag{6}$$

where $\hat{H}_{\rm loc}$ is the Hamiltonian of interaction of local magnetic field with the bismuth nuclear magnetic moment, $\hat{H}_{\rm e}$ is the Hamiltonian of interaction of external magnetic field with the bismuth nuclear magnetic moment

$$\begin{aligned}\hat{H}_{\rm loc} &= -g_{\rm Bi}\mu_{\rm B}\boldsymbol{H}_{\rm loc}\boldsymbol{I} = \\ &= -g_{\rm Bi}\mu_{\rm B}H_{\rm loc}(\sin\theta_{\rm loc}\cos\varphi_{\rm loc}\, I_{x'} + \\ &\quad + \sin\theta_{\rm loc}\sin\varphi_{\rm loc}\, I_{y'} + \cos\theta_{\rm loc}\, I_{z'}),\end{aligned} \tag{7}$$

$$\hat{H}_e = -g_{\rm Bi}\mu_{\rm B}\boldsymbol{H}_{\rm e}\boldsymbol{I} = -g_{\rm Bi}\mu_{\rm B}H_{\rm e}(D_{13}I_{x'} + D_{23}I_{y'} + D_{33}I_{z'}). \tag{8}$$

Here $g_{\rm Bi} = \mu_{\rm Bi}/I\mu_{\rm B}$, $\mu_{\rm Bi} = 4.0797\mu_{\rm B}$ is the magnetic moment of the bismuth nucleus and angles $\theta_{\rm loc}$ and $\varphi_{\rm loc}$ determine the direction of $\boldsymbol{H}_{\rm loc}$ with respect to the EFG principal axes.[12]

In $\boldsymbol{H}_{\rm e} \perp \boldsymbol{H}_{\rm rf}$, the components of the matrix D are

$$\begin{aligned}D_{13} &= \cos\psi\ \sin\varphi\ \sin\alpha + \\ &\quad + \sin\psi\ (\cos\theta\ \cos\varphi\ \sin\alpha + \sin\theta\ \cos\alpha), \\ D_{23} &= -\sin\psi\ \sin\varphi\ \sin\alpha + \\ &\quad + \cos\psi\ (\cos\theta\ \cos\varphi\ \sin\alpha + \sin\theta\ \cos\alpha), \\ D_{33} &= -\sin\theta\ \cos\varphi\ \sin\alpha + \cos\theta\ \cos\alpha.\end{aligned} \tag{9}$$

Hence, in this case, the nuclear spin energy levels E_j ($j = 1, 2, \ldots, 10$) are determined by the parameters eQq/h, $H_{\rm loc}$, $\theta_{\rm loc}$, $\varphi_{\rm loc}$, $H_{\rm e}$, θ, φ and α.

In $H_{\rm loc} = 0$ and $\eta = 0$, the typical Zeeman spectrum consists of a quadruplet assigned to the transition ν_1 ($\Delta m = 1/2-3/2$) and doublets for the remaining transitions, provided that all the EFG tensors are magnetically equivalent (see, for instance, Fig. 4 in Ref. 12). As follows from Eqns (6), (8) and (9), the contribution of the external magnetic field ($\boldsymbol{H}_{\rm e} \perp \boldsymbol{H}_{\rm rf}$) to the splitting of the doublet components is determined as

$$\Delta_{\rm e} = \frac{2g_{\rm Bi}\mu_{\rm B}}{h}H_{\rm e}(-\sin\theta\ \cos\varphi\ \sin\alpha + \cos\theta\ \cos\alpha). \tag{10}$$

It can be shown that in $\boldsymbol{H}_{\rm e} \,||\, \boldsymbol{H}_{\rm rf}$, the matrix D does not depend on α, and the above expression becomes

$$\Delta_{\rm e} = \frac{2g_{\rm Bi}\mu_{\rm B}}{h}H_{\rm e}\sin\theta\ \sin\varphi. \tag{11}$$

Using Eqns (10), (11) with relationships (4) taken into account, one can simulate the Zeeman-perturbed ^{208}Bi NQR spectra for the $Bi_4Ge_3O_{12}$ single crystal. The splittings of the selected lines in the Zeeman spectrum of this crystal are shown in Fig. 4. As follows from Eqn (11), the Zeeman-perturbed patterns assigned to the transition $\Delta m = 3/2-5/2$ and other higher transitions in $\boldsymbol{H}_{\rm e} \,||\, \boldsymbol{H}_{\rm rf}$ are expected to be unit doublets, because the separations between the doublet components are identical according to relationships (4) for all the four EFG tensors. Meanwhile, it is clearly seen in Fig. 4 *c* that each doublet component displays a weak additional splitting, which can be explained by the presence of $H_{\rm loc}$ in the compound $Bi_4Ge_3O_{12}$. The contribution of $H_{\rm loc}$ to the Zeeman splitting of the NQR spectra is described by the formula

$$\Delta_{\rm loc} = \frac{2g_{\rm Bi}\mu_{\rm B}H_{\rm loc}\cos\theta_{\rm loc}}{h}. \tag{12}$$

The net splitting observed between the doublet components for the transitions $\nu_2-\nu_4$ is evidently constituted by a superposition of the contributions described by Eqns (11) and (12):

$$\Delta = |\Delta_{\rm e} + \Delta_{\rm loc}|. \tag{13}$$

Analysis of the Zeeman-perturbed pattern for the line ν_2, carried out using Eqns (11)–(13), showed that the simulated pattern gives the best fit to the observed one (compare Figs 4 *c* and *f*) if the local magnetic fields are added to relationships (4) for the angular parameters of the EFG principal axes as follows:

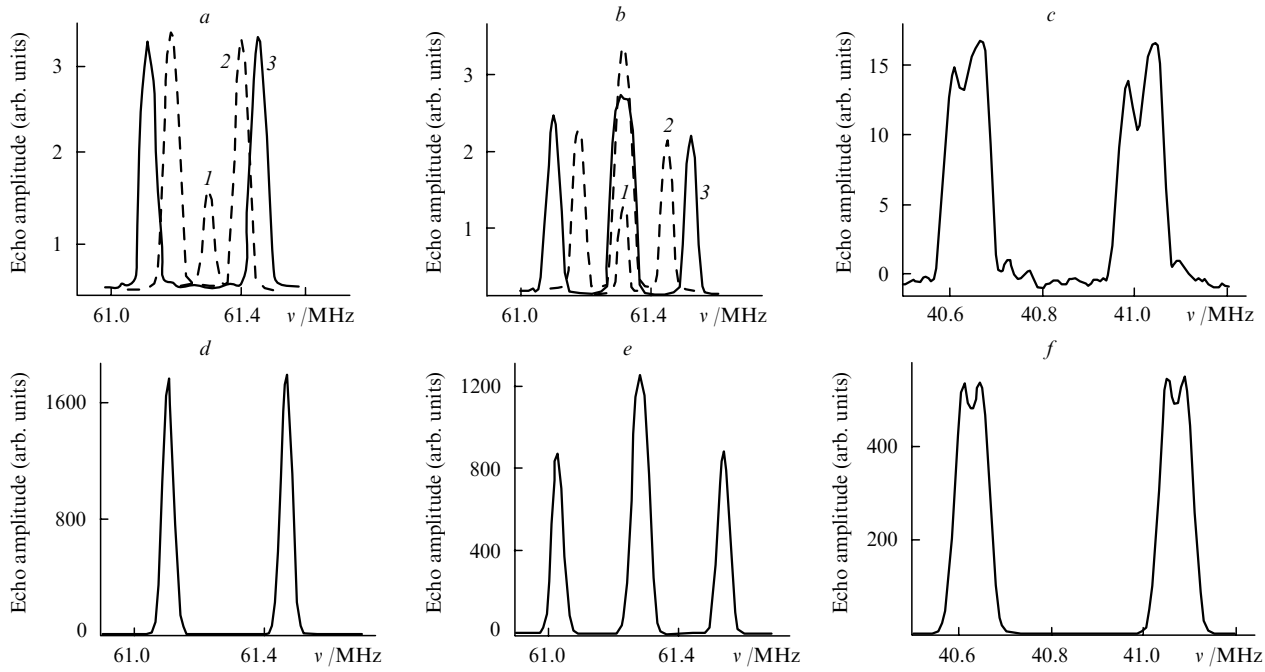


Figure 4. Recorded ($a-c$) and simulated ($d-f$) Zeeman-perturbed patterns in the ^{209}Bi NQR spectrum of the $Bi_4Ge_3O_{12}$ single crystal; (a, d) are the lines assigned to the transition ν_3 ($\Delta m = 5/2-7/2$) in the field $\boldsymbol{H}_e \perp \boldsymbol{H}_{rf}$ at the orientation of the crystal $\alpha = 0^\circ$ (see text); (b, e) $\alpha = 45^\circ$; (c, f) are the lines assigned to the transition ν_2 ($\Delta m = 3/2-5/2$) in the field $\boldsymbol{H}_e \,||\, \boldsymbol{H}_{rf}$. H_e /Œ: (a, b) 0 (*1*), 300 (*2*), 480 (*3*); (c, f) 450; (d, e) 480.

$$\theta,\ \varphi,\ H_{loc}\cos\theta_{loc};\quad \pi-\theta,\ \varphi,\ -H_{loc}\cos\theta_{loc};\qquad (14)$$
$$\theta,\ \pi-\varphi,\ H_{loc}\cos\theta_{loc};\quad \pi-\theta,\ \pi-\varphi,\ -H_{loc}\cos\theta_{loc}\,.$$

This means that the local magnetic fields in the compound $Bi_4Ge_3O_{12}$ are ordered antiferromagnetically. The magnitude of projection $H_{loc}\cos\theta_{loc}$ of the local field vector onto the EFG principal axis z', estimated from the additional splittings of the doublet components in $\boldsymbol{H}_e \,||\, \boldsymbol{H}_{rf}$ (Fig. 4 *c*), was found to amount to 30 ± 5 Œ.

The angular parameters θ and φ can be found using Eqn (10) from the analysis of the Zeeman-perturbed line shapes observed upon rotation of the single crystal in the radiofrequency coil ($\boldsymbol{H}_e \perp \boldsymbol{H}_{rf}$) through various angles α. Thus, it follows from this equation that the Zeeman-perturbed pattern at $\alpha = 0^\circ$ is a doublet, which was confirmed experimentally (Fig. 4 *a*). Using Eqn (10) and the experimental data, the angle θ was found to amount to $61 \pm 3^\circ$.

It also follows from equation (10) that the Zeeman patterns should be identical at α equal to $+45$, -45 and -135. The coincidence of the appropriate splittings has earlier been observed experimentally as well.[12] The angle $\varphi = 54 \pm 3^\circ$ was determined using Eqn (10) from the measured separation between the outer pair of lines in the Zeeman spectra (see Figs. 4 *a*, *b*). A more complicated modelling procedure [12] had to be performed because of slight deviation of the crystallographic axis of the sample from the $\boldsymbol{H}_{rf}$ direction due to the imperfect shape of the single crystal used for the experiment.

The probability of transitions between the nuclear spin energy levels Y_i is proportional to the squared matrix element

$$\Omega_{ij} = |\langle Y_i|\boldsymbol{H}_{rf}\boldsymbol{I}|Y_j\rangle|^2 = H_{rf}^2\,\omega_{ij}\,, \qquad (15)$$

where for both cases, $\boldsymbol{H}_e \,||\, \boldsymbol{H}_{rf}$ and $\boldsymbol{H}_e \perp \boldsymbol{H}_{rf}$ the relationships

$$\omega_{ij} = |\langle Y_i|D_{11}I_{x'} + D_{21}I_{y'} + D_{31}I_{z'}|Y_j\rangle|^2, \qquad (16)$$

$$D_{11} = \cos\psi\cos\varphi - \mathrm{sinc}\cos\theta\sin\varphi,$$

$$D_{21} = -\sin\psi\cos\varphi - \cos\psi\cos\theta\sin\varphi,$$

$$D_{31} = \sin\theta\sin\varphi$$

hold true.

The line shape was modelled by a procedure described earlier [4]:

$$F_{ij} \propto \nu_{ij}^2\omega_{ij}\int_{\tilde{\nu}_1}^{\tilde{\nu}_2} g(\nu-\nu_{ij})\mathrm{d}\nu. \qquad (17)$$

Here $\nu_{ij} = (E_j - E_i)/h$ is transition frequency, ω_{ij} is defined by Eqn (16) and Gaussian $g(\nu-\nu_{ij})$ is described as

$$g(\nu-\nu_{ij}) = \frac{\sqrt{4\ln 2}}{\sqrt{\pi}\sigma}\exp\left[-\frac{4\ln 2(\nu-\nu_{ij})^2}{\sigma^2}\right], \qquad (18)$$

where σ denotes a line width at half maximum and simulates the effect of broadening due to EFG inhomogeneity.

The entire spectrum was simulated by summing the functions (17) over all the transitions with non-zero ω_{ij}

$$F = \sum_{i,j} F_{ij}\,. \qquad (19)$$

As was said above, the observed splittings in Fig. 4 (see also Figs 1 and 2 in Ref. 12) represent a superposition of the Zeeman splittings giving rise to a complicated pattern that depends on the orientation of $\boldsymbol{H}_e$ with respect to the crystal axes (angle α) and direction of $\boldsymbol{H}_{rf}$. In $\boldsymbol{H}_e \,||\, \boldsymbol{H}_{rf}$, the spectral pattern is independent of the position of a sample in a probe head and remains unchanged upon rotation of the crystal. In $\boldsymbol{H}_e \perp \boldsymbol{H}_{rf}$, the spectral patterns recorded at α equal to -135 and $\pm 45^\circ$ were similar to each other as well as those at 0 and -90° [here ($-$) means clockwise and ($+$), counterclockwise rotation].[12]

Therefore, based on the results of computer simulation of the Zeeman splittings in the ^{209}Bi NQR spectra of the $Bi_4Ge_3O_{12}$ single crystal, the conclusion was made that antiferromagnetically ordered local magnetic fields of the order of 30 Œ exist in the unit cell of this compound.[12]

Apart from the additional splittings caused by the local magnetic fields, the Zeeman spectra of $Bi_4Ge_3O_{12}$ exhibited yet another specific feature: a dramatic increase in the resonance intensity occurred in an external magnetic field (see Fig. 4). The resonance line intensity is known to be proportional to

$$I \approx \nu_{ij}^2 \omega_{ij},$$

where ν_{ij} is the frequency of transition between the quadrupole levels i and j, and ω_{ij} is the term that defines the angular dependence of the transition probability [see Eqn (16)]. This term seems to be the only factor that can vary considerably upon applying $\boldsymbol{H}_e$. Therefore, the angular dependence of the resonance intensity for the $\nu_2 - \nu_4$ transitions was analysed.[12] This is determined by the sum of the squared coefficients of $I_{x'}$ and $I_{y'}$ in Eqn (16) as

$$S = \cos^2\theta + \sin^2\theta \cos^2\varphi. \qquad (20)$$

Assuming the angular dependence of the function S to be responsible for the observed increase in intensity, one has to admit that $\boldsymbol{H}_e$ is capable of influencing the spatial orientation of the EFG axes with respect to the crystallographic ones.[12]

As distinct from $Bi_4Ge_3O_{12}$, no splittings were observed in the zero-field ^{209}Bi NQR spectrum of the $Bi_3B_5O_{12}$ single crystal. However, the anomalies found in the intensity ratio of the spectroscopic lines suggested the presence of unusual magnetic properties in this compound as well.[13] The $Bi_3B_5O_{12}$ single crystal used in the experiment was grown by the Czochralski method from a stoichiometric melt to have a long side (20 mm) parallel to the b-axis of the unit cell and a hexagonal cross-section ($D \cong$ 10 mm). The plane parallel to the ab-plane of the crystal was polished. According to the X-ray data,[16,17] the orthorhombic (space group $Pnma$) lattice of bismuth borate comprises two crystallographically independent bismuth sites [Bi(1) and Bi(2)] that form a triangle centred at the oxygen atom not bonded to boron atoms (Fig. 5). The occupancy of the Bi(2) position of the general type is evidently twice as high as that of Bi(1) lying in the symmetry element (the mirror plane). In agreement with the X-ray diffraction data, the ^{209}Bi NQR spectrum of $Bi_3B_5O_{12}$ also points to the presence of two crystallographically independent bismuth positions. The Bi(1) atom, located in the mirror plane, is characterised by lesser magnitude of the EFG asymmetry parameter than Bi(2) due to its higher local symmetry (Table 2). The double occupancy of the Bi(2) sites is expected to give, in the NQR spectrum, the line ν_2 of nearly double intensity as compared to ν_2 of Bi(1).

However, the experiment on a single crystal showed the inverse resonance intensity ratio: the intensity of the ν_2 line of Bi(1) lying in the mirror plane was at least twice as high as that assigned to Bi(2) in the general position (Fig. 6).

In order to calculate the dependence of the resonance intensities in a pure NQR spectrum of a single crystal on the orientation of the EFG axes with respect to the $\boldsymbol{H}_{rf}$ direction one has to find the orientation of these axes at both bismuth sites with respect to the crystal axes. For this, the zero-field resonance intensities were

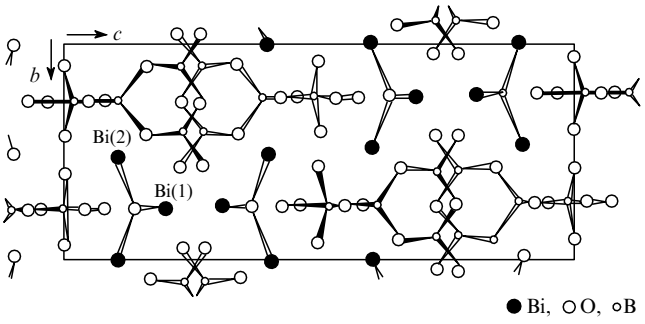


Figure 5. Projection of the $Bi_3B_5O_{12}$ crystal structure along the crystallographic axis a.[17]

Table 2. The zero-field ^{209}Bi NQR spectrum of $Bi_3B_5O_{12}$ at 300 K.[18]

Atom	Transition frequencies /MHz				eQq/h /MHz	η (%)
	ν_1	ν_2 (see [a])	ν_3	ν_4		
Bi(1)	35.50	53.03 (0.55)	82.09	109.90	661.4	19.3
Bi(2)	71.60	52.20 (1)	72.20	101.50	632.7	65.7

[a] The resonance intensities calculated on the basis of the X-ray diffraction data[16] are parenthesised.

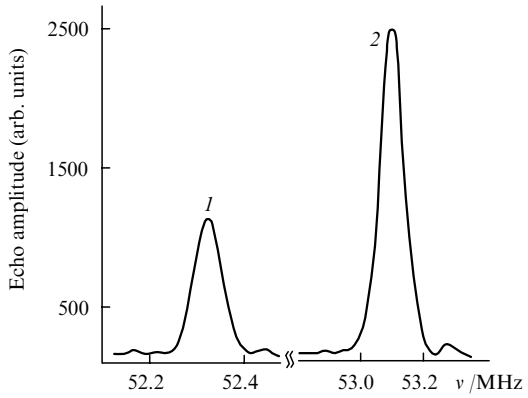


Figure 6. Zero-filed ν_2 resonances assigned to the sites Bi(2) (*1*) and Bi(1) (*2*) in the ^{209}Bi NQR spectrum of the $Bi_3B_5O_{12}$ single crystal ($\boldsymbol{H}_{rf} \| b$).

first analysed on rotation of the crystal about the b-axis in $\boldsymbol{H}_{rf} \perp b$ (Fig. 7) and then the Zeeman-perturbed NQR spectra were examined in the external magnetic field optimum for modelling

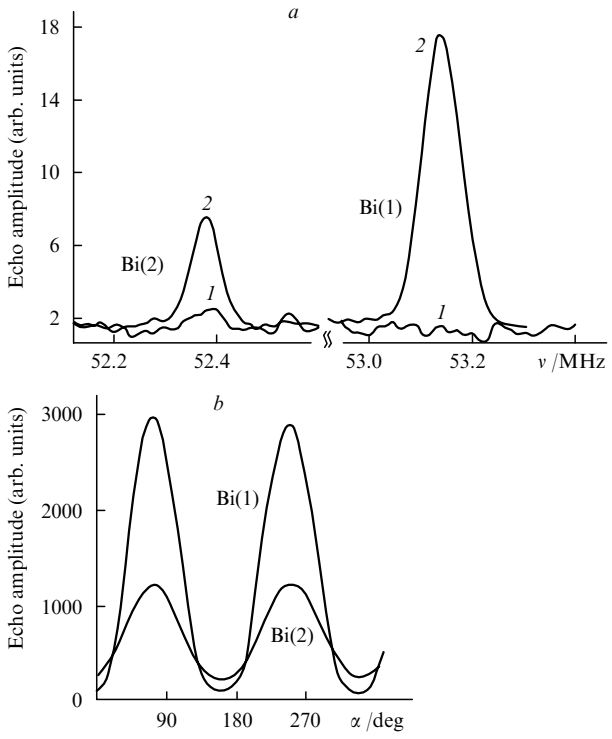


Figure 7. Zero-field ν_2 resonances assigned to the sites Bi(1) and Bi(2) in the ^{209}Bi NQR spectrum of the $Bi_3B_5O_{12}$ single crystal for the crystal orientation $\boldsymbol{H}_{rf} \perp b$, $\boldsymbol{H}_{rf} \| a$ (*1*) and $\boldsymbol{H}_{rf} \perp b$, $\boldsymbol{H}_{rf} \| c$ (*2*) (*a*) and the amplitude changes of these resonances over one-period rotation of the crystal about the crystallographic axis b ($\boldsymbol{H}_{rf} \perp b$) (*b*).

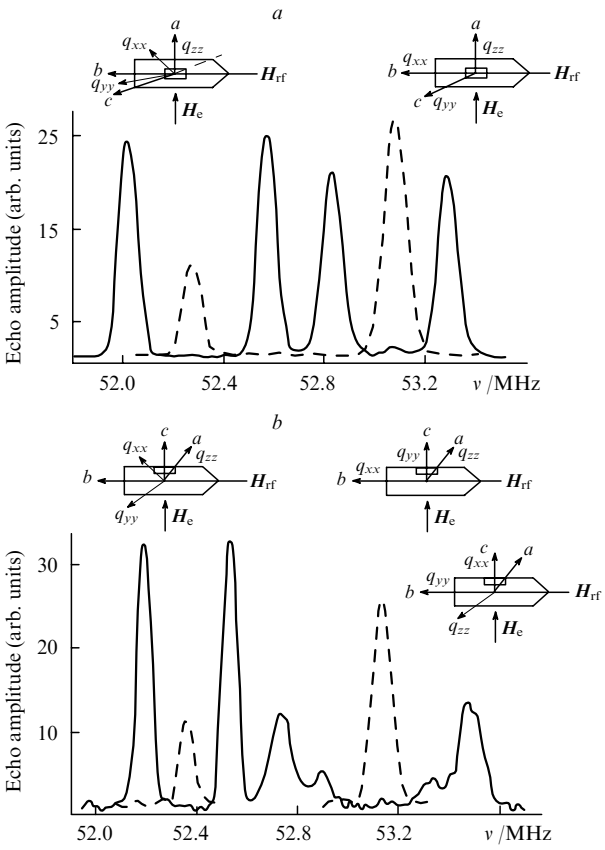


Figure 8. Zeeman-perturbed ($\boldsymbol{H}_e \perp \boldsymbol{H}_{rf}$, H_e = 300 Œ) ν_2 resonances (see Table 2) in the ^{209}Bi NQR spectrum of the $Bi_3B_5O_{12}$ single crystal (solid lines) as compared to those in zero magnetic field (dotted lines) for the crystal orientations $\boldsymbol{H}_{rf} \| b$, $\boldsymbol{H}_e \| q_{zz} \| a$ (*a*) and $\boldsymbol{H}_{rf} \| b$, $\boldsymbol{H}_e \| c$ (*b*). The orientations of the crystallographic and EFG principal axes of the single crystal as well as the directions of the $\boldsymbol{H}_e$ and $\boldsymbol{H}_{rf}$ fields are given for the Bi(1) and Bi(2) sites.

(H_e = 300 Œ) at two orientations of the crystal with respect to the $\boldsymbol{H}_e$ direction (Fig. 8).[13] In zero field, the rotation of the sample in the rf-coil about the *b*-axis was accompanied by a simultaneous amplitude change for both resonances: they practically vanished in $\boldsymbol{H}_{rf} \| a$ and reached their maxima in $\boldsymbol{H}_{rf} \| c$, whereas the intensity ratio

$$r = \frac{I_{Bi(1)}}{I_{Bi(2)}} \tag{21}$$

at its maximum remained the same ($r > 2$, see Fig. 7 *b*). This means that on both bismuth sites, the EFG q_{zz} axes are parallel to the crystallographic axis *a*. The orientations of the q_{xx} and q_{yy} axes with respect to the crystal axes were found from the Zeeman experiment in H_e = 300 Œ ($\boldsymbol{H}_e \perp \boldsymbol{H}_{rf}$; $\boldsymbol{H}_{rf} \| b$). The splittings ($\Delta\nu$) between the Zeeman components for both Bi(1) and Bi(2) atoms at various positions of the crystal in the probe head (see Fig. 8) are given by the formula

$$\Delta\nu = 2\gamma H_e \left\{ \left[A_m \cos^2\theta + \frac{1}{4}\sin^2\theta \,(B_m + 2C_m \cos 2\varphi) \right]^{1/2} - \right. \tag{22}$$
$$\left. - \left[A_{m'} \cos^2\theta + \frac{1}{4}\sin^2\theta \,(B_{m'} + 2C_{m'} \cos 2\varphi) \right]^{1/2} \right\},$$

where $\pm m$ and $\pm m'$ denote the degenerate states $\pm 3/2$ and $\pm 5/2$, respectively, and the coefficients $A_{m(m')}$, $B_{m(m')}$, $C_{m(m')}$ are tabulated by Cohen for certain values of η.[19] Good agreement of the observed and calculated splittings (Table 3) is reached assuming that at Bi(1), the EFG $q_{xx}(q_{yy})$ axis is parallel to the *b*-axis and

Table 3. The observed ($\Delta\nu_{exp}$) and calculated ($\Delta\nu_{calc}$) splittings of the ν_2 resonances in the ^{209}Bi NQR spectrum of the $Bi_3B_5O_{12}$ single crystal in H_e = 300 Œ (see Fig. 8).[13]

Atom	ν_2 /MHz	$\Delta\nu_{exp}$ /kHz	$\Delta\nu_{calc}$ /kHz
		$\boldsymbol{H}_e \| a$	
Bi(1)	53.03	466.0	487.0
Bi(2)	52.20	548.0	566.0
		$\boldsymbol{H}_e \| c$	
Bi(1)	53.03	548.0 (av.)	554.5 (av.)
Bi(2)	52.20	342.0	389.0

$q_{yy}(q_{xx})$, to the *c*-axis of the crystal. At Bi(2), q_{xx} lies in the *bc*-plane at an angle of 45° to the *b*-axis and q_{yy}, in the same plane at an angle of −45° to the *b*-axis. The additional splitting of the ν_2 Bi(1) line (see Fig. 8 *b*) is caused by the magnetically non-equivalent Bi(1) positions in the lattice. With the orientation of the EFG principal axes found, one can calculate the expected resonance intensity ratio *r* in zero field, *i.e.*, in a pure quadrupole spectrum of a single crystal. The transition probability *W* (and hence the line intensity) in a pure NQR spectrum is known to depend on the orientation of the EFG axes with respect to the $\boldsymbol{H}_{rf}$ direction as

$$W = 2D\cos^2\theta + \frac{1}{2}\sin^2\theta \left(G + 2J\cos 2\varphi\right). \tag{23}$$

Here θ and φ are the angles between the $\boldsymbol{H}_{rf}$ direction and the EFG principal axes; *D*, *G* and *J* are the coefficients depending on η and *m*.[19] As the results of the calculation showed, the resonance intensity ratio *r* in a pure NQR spectrum is less than unity being different in the crystal orientations $\boldsymbol{H}_{rf} \perp b$ and $\boldsymbol{H}_{rf} \| b$. However, the experimental intensity ratio *r* exceeded 2 and was the same in both crystal orientations (see Figs 6 and 7). Hence, the observed zero-field NQR spectrum of the $Bi_3B_5O_{12}$ single crystal is not a pure quadrupole spectrum, which gives indirect evidence for the existence of unusual magnetism-related properties in this compound, in particular, local magnetic fields found earlier in α-Bi_2O_3 and $Bi_4Ge_3O_{12}$. These fields are most likely weak, so that the appropriate zero-field splittings are masked by the effect of inhomogeneous line broadening and cannot be observed directly. The Zeeman fields H_e = 300 Œ optimal for modelling completely suppressed the spectroscopic manifestation of the local field ($H_e \gg H_{loc}$), resulting in no anomalies in the Zeeman splittings. Therefore, the evaluation of the local field strength and orientation with respect to the crystal axes from the Zeeman experiments appeared impossible.[13]

IV. Studies of local magnetic fields by analysis of the quadrupole spin echo envelope

A study of the problem was continued using an approach enabling detection of weak (within an inhomogeneous line broadening) spectroscopic splittings. Such splittings are known to be registered as low-frequency modulations of the spin echo envelope. The registering of SEE involves accumulation of the NQR signals upon continuous increase in pulse separation followed by data processing. A preliminary experiment showed that the SEE for the ν_2 Bi(1) line was modulated in zero field, pointing to the presence of line splitting. A detailed examination of this SEE curve revealed its distinctive modulation in both single crystal and powder samples of $Bi_3B_5O_{12}$ (Fig. 9).[13] The strength and orientation of $\boldsymbol{H}_{loc}$ had to be further evaluated from the SEE shape using the mathematical model. However, due to the low-symmetry structure of $Bi_3B_5O_{12}$, an increased multiplicity of the spectrum occurs in external magnetic field, thus revealing the magnetic non-equivalence of the bismuth sites. In order to avoid computational difficulties, a model [13] was first elaborated for $Bi_2Ge_3O_9$ [benitoite-type structure, space group $P6_3/m$ (see Ref. 11)], the

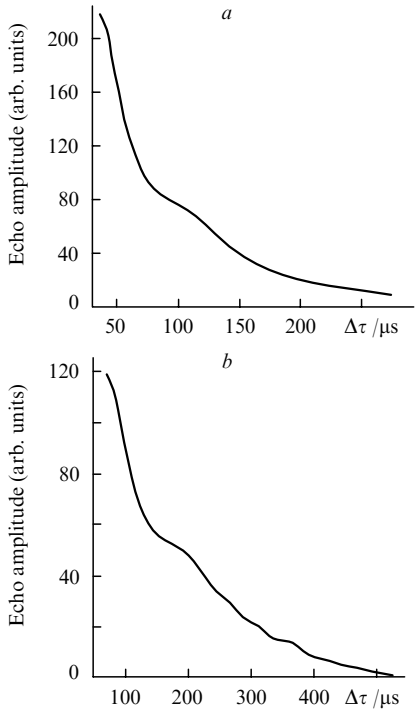


Figure 9. Zero-field spin echo envelopes assigned to the ν_2 transition of Bi(1) (see Table 2) recorded for the $Bi_3B_5O_{12}$ single crystal at ambient temperature (*a*) and for a powder sample at 77 K (*b*).[13]

^{209}Bi NQR spectrum of which is given in Table 1. In agreement with the X-ray diffraction data, the spectrum reveals an axial symmetry of the crystallographically equivalent bismuth sites ($\eta = 0$, see Table 1). Earlier, the existence of local magnetic field in this compound has been suggested based on the analysis of the zero-field line shape (Fig. 10).[4]

As follows from the symmetry properties of the EFG tensor at the ^{209}Bi sites, the lattice charge contribution to the EFG tensor is the same for all the bismuth atoms in the unit cell of $Bi_2Ge_3O_9$, *i.e.*, all the bismuth positions are crystallographically and magnetically equivalent. Hence, its ^{209}Bi NQR spectrum gives a single set of splittings in a magnetic field.[13] In addition, the EFG principal axis q_{zz} is parallel to the sixfold axis of the hexagonal lattice, which is the *z*-axis of the crystal.

The zero-field SEE curves were recorded at room temperature for the lines assigned to the ν_1 and ν_2 transitions[13] (see Table 1) using a powder sample of $Bi_2Ge_3O_9$ prepared as described in Ref. 3 (see Fig. 11). In zero external field, the SEE curve assigned

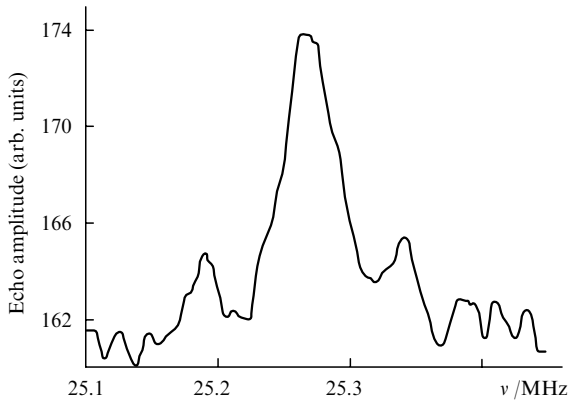


Figure 10. A zero-field line assigned to the transition ν_1 ($\Delta m = 1/2-3/2$) in the ^{209}Bi NQR spectrum of a powder sample of $Bi_2Ge_3O_9$.

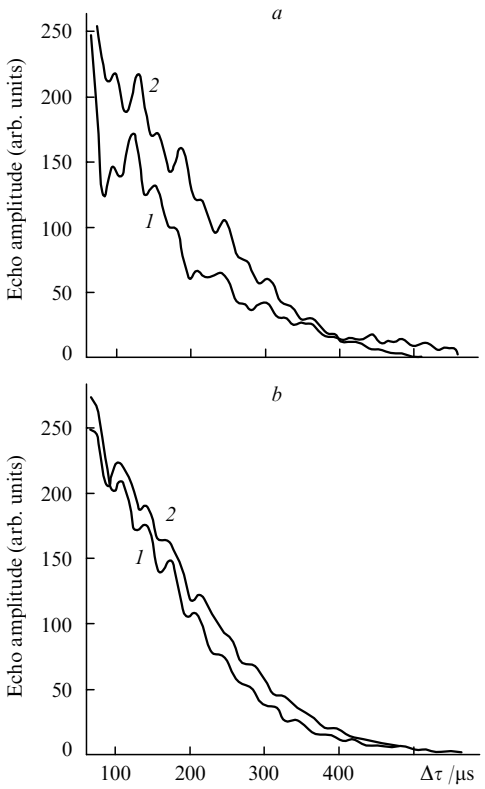


Figure 11. Observed (*1*) and calculated (*2*) zero-field spin echo envelopes assigned to the transitions ν_1 ($\Delta m = 1/2-3/2$) (*a*) and ν_2 ($\Delta m = 3/2-5/2$) (*b*) for a powder sample of $Bi_2Ge_3O_9$.[13]

to the ν_2 transition exhibits apparently regular oscillations, whereas the modulation pattern of the SEE curve assigned to the ν_1 line is more complicated, both indicating the presence of a local magnetic field in this compound. The evaluation of the local field characteristics was performed by modelling of the SEE that took into account the presence of local and external magnetic fields.[13] Like the model described earlier[20] where the SEE was analysed for nuclei with the spin 3/2, this approach was based on the density matrix formalism with the difference consisting in the consideration of the symmetry properties of the EFG and local magnetic field that substantially influence the SEE shape.[13] The basic stages of the modelling[13] as well as the algorithm for the SEE calculation in the presence of $\boldsymbol{H}_e$ and $\boldsymbol{H}_{loc}$ are given in the Appendix.

The simulated SEE curves are also shown in Fig. 11. It was found that the shape of the simulated curve assigned to the ν_1 transition was in fairly good agreement with the experimental one assuming that the local magnetic field in $Bi_2Ge_3O_9$ amounts to 65 ± 5 G and directed at an angle $83 \pm 1^\circ$ to the EFG q_{zz}-axis. As to the transitions higher than ν_1, their line shapes are expected to be featureless in the external magnetic field, if $\eta = 0$ (Refs 20 and 21). In agreement with the results of studies,[21] the simulated lines uniformly broadened to the Larmor frequency value. However, the results of modelling[13] showed that, assuming even negligibly small deviation of the EFG symmetry from the axial ($\eta \sim 0.005$), the modulations of the SEE curve assigned to the ν_2 transition are closely reproduced at the same characteristics of H_{loc} that have been found from the modelling of the SEE assigned to the ν_1 transition (see Fig. 11). Naturally, such a small value of η is beyond the accuracy of NQR measurements. The question on whether the appropriate deviation of the electron density distribution from axial symmetry might be detected in an X-ray experiment seems to be interesting. The anomalies found in the magnetic properties of $Bi_2Ge_3O_9$ make the experiments on a single crystal very attractive. Unfortunately, all efforts to grow a single crystal of suitable size failed.[13]

The modelling of the SEE for $Bi_3B_5O_{12}$ having more complicated structure was carried out in a similar way (Fig. 12). As was mentioned above, the unit cell of $Bi_3B_5O_{12}$ is orthorhombic [space group *Pnma* (D_{2h}^{16}), $Z = 2$] with four Bi(1) atoms occupying the *c*-sites in the symmetry plane and eight Bi(2) atoms, the *d*-positions of the general type.[16, 17] The analysis of the EFG symmetry at the *c*-sites showed that two types of the EFG tensors are available for the $Bi_1(1)$, $Bi_2(1)$ and $Bi_3(1)$, $Bi_4(1)$ atoms, respectively:

$$\begin{pmatrix} a & 0 & d \\ 0 & b & 0 \\ d & 0 & c \end{pmatrix} \text{ (I) and } \begin{pmatrix} a & 0 & -d \\ 0 & b & 0 \\ -d & 0 & c \end{pmatrix} \text{ (II),}$$

where *a*, *b*, *c*, *d* are the lattice sums of products of the atomic coordinates by derivatives of the crystal-field potentials at the atomic sites.[7] The roots of the characteristic equations associated with the tensors (I) and (II) are equal to each other

$$\lambda_1 = b, \tag{24}$$

$$\lambda_{2,3} = \frac{a+c}{2} \pm \frac{1}{2}\sqrt{(a-c)^2+4d^2}.$$

The fact that one of the roots is equal to the diagonal element of the EFG tensor ($\lambda_1 = b$) complicates the procedure of finding the direction cosines for the principal axes of the tensors (I) and (II). However, one can show that the following symmetry relationships hold true:

$$\sigma_{21}^{(I)} = \sigma_{31}^{(II)},\ \sigma_{31}^{(I)} = \sigma_{21}^{(II)},\ \sigma_{23}^{(I)} = -\sigma_{33}^{(II)},\ \sigma_{33}^{(I)} = -\sigma_{23}^{(II)},$$

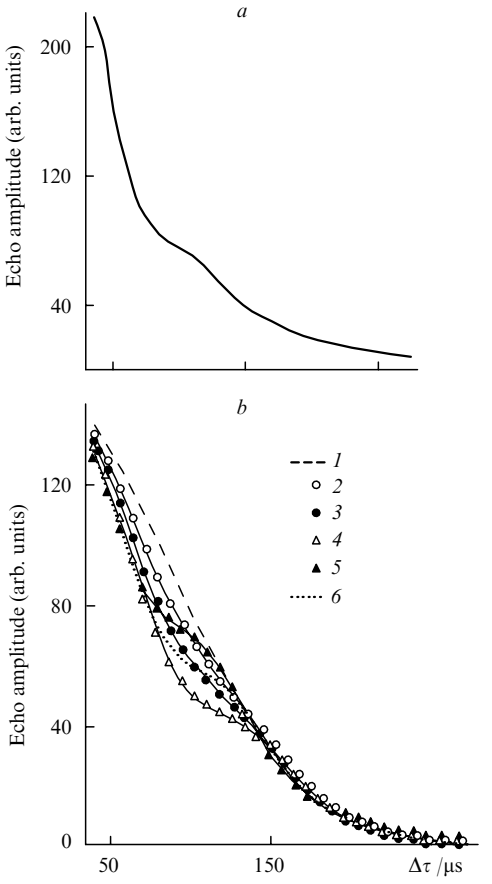


Figure 12. Observed (*a*) and simulated (*b*) SEE curves of the transition ν_2 of the Bi(1) site in the ^{209}Bi NQR spectrum of the $Bi_3B_5O_{12}$ single crystal for the various parameters of local magnetic field ($H_{loc\,i} = H_{loc}\cos\theta_i$).
$H_{loc\,i}$/Œ: 0 (*1*), 2 (*2–4*), 2.5 (*5*), 2.25 (*6*);
θ_i/deg: 0 (*1*), 15 (*2*), 20 (*3*, *5*), 25 (*4*), 22.5 (*6*).

$$\sigma_{12}^{(I)} = \sigma_{12}^{(II)} = 1 \tag{25}$$

$$\sigma_{11}^{(I)} = \sigma_{13}^{(I)} = \sigma_{22}^{(I)} = \sigma_{32}^{(I)} = \sigma_{11}^{(II)} = \sigma_{13}^{(II)} = \sigma_{22}^{(II)} = \sigma_{32}^{(II)} = 0.$$

These relationships enable one to determine the two of three Euler angles connecting the crystallographic coordinate system with those of the EFG principal axes (see Fig. 3 *b*).

$$\theta_1, \varphi_1 = \frac{3\pi}{2}, \quad \psi_1 = \frac{\pi}{2}, \tag{26}$$

$$\theta_2 = \theta_1 + \frac{\pi}{2}, \quad \varphi_2 = \frac{\pi}{2}, \quad \psi_2 = \frac{3\pi}{2}.$$

The θ_1-value for the Bi(1) positions in the $Bi_3B_5O_{12}$ lattice can be found from a comparison of the simulated and observed NQR Zeeman spectra.[13] The modelling of the Zeeman spectra was performed as described above (see Part III). For the $Bi_3B_5O_{12}$ single crystal used in the experiments, the components of the rotation matrix *D* in the Hamiltonian $\hat{H}_e$ [see Eqn (8)] are

$$\begin{aligned} D_{13} &= -\cos\psi\ \cos\varphi\ \sin\alpha + \\ &\quad + \sin\psi\ (\cos\theta\ \sin\varphi\ \sin\alpha + \sin\theta\ \cos\alpha), \\ D_{23} &= \sin\psi\ \cos\varphi\ \sin\alpha + \\ &\quad + \cos\psi\ (\cos\theta\ \sin\varphi\ \sin\alpha + \sin\theta\ \cos\alpha), \\ D_{33} &= -\sin\theta\ \sin\varphi\ \sin\alpha + \cos\theta\ \cos\alpha, \end{aligned} \tag{27}$$

where θ, φ and ψ are the Euler angles [see Eqn (26)]. It is to be reminded that the field $\boldsymbol{H}_{rf}$ was parallel to the axis *b* of the single crystal, and the crystal was turned through the angle α about the coil axis coinciding with the $\boldsymbol{H}_{rf}$ direction. At $\alpha = 0^\circ$, the external field $\boldsymbol{H}_e$ was directed along the *c*-axis, and at $\alpha = -90^\circ$, along the *a*-axis of the crystal. In $\boldsymbol{H}_e \,||\, c$ ($\alpha = 0^\circ$), the components of the rotation matrices in Eqn (27) referring to the two sets of the Euler angles (26) are described as

$$\begin{aligned} &D_{13}^{(1)} = \sin\theta_1, \quad D_{23}^{(1)} = 0, \quad D_{33}^{(1)} = \cos\theta_1, \\ &D_{13}^{(2)} = -\cos\theta_1, \quad D_{23}^{(2)} = 0, \quad D_{33}^{(2)} = -\sin\theta_1. \end{aligned} \tag{28}$$

In these expressions, the upper index corresponds to the set of the angular parameters in Eqn (26). In $\boldsymbol{H}_e \,||\, a$ ($\alpha = -90^\circ$), the components of the rotation matrices become

$$\begin{aligned} &D_{23}^{(1)} = 0, \quad D_{33}^{(1)} = -\sin\theta_1, \\ &D_{13}^{(2)} = -\sin\theta_1, \quad D_{23}^{(2)} = 0, \quad D_{33}^{(2)} = \cos\theta_1. \end{aligned} \tag{29}$$

The angle $\theta_1 = 0 \pm 5^\circ$ was found from the comparison of the observed (Fig. 8) and simulated spectra of the $Bi_3B_5O_{12}$ single crystal in $H_e = 300$ Œ.

The calculation of the SEE shape by the program based on the density matrix formalism [13] (see Appendix) enabled one to derive the value of local magnetic field in this compound ($\sim$2.5 G, see Fig. 12).

Thus, the above results showed that a weak local magnetic field exists in $Bi_3B_5O_{12}$. Assuming that the presence of these fields is related to the anomalies observed for the resonance intensity ratio [for instance, the local field unequally influences the intensities assigned to the ν_2 resonances assigned to the Bi(1) and Bi(2) sites characterised by the EFG of presumably different symmetry [13]], one has to admit the existence of a strong coupling between the electronic and magnetic subsystems in $Bi_3B_5O_{12}$.

The zero-field modulations of the ^{209}Bi SEE curves were naturally observed in the compounds where $\boldsymbol{H}_{loc}$ has earlier been revealed from either Zeeman-perturbed or zero-field spectroscopic splittings.[13] Distinctive modulations were also observed for $BaBiO_2Cl$ (Fig. 13) the crystallochemical properties of which have much in common with those of the above described Bi_3O_4Br. In the structures of both compounds, the layers of bismuth oxide polyhedra alternate with those of halide anions.[22, 23] The

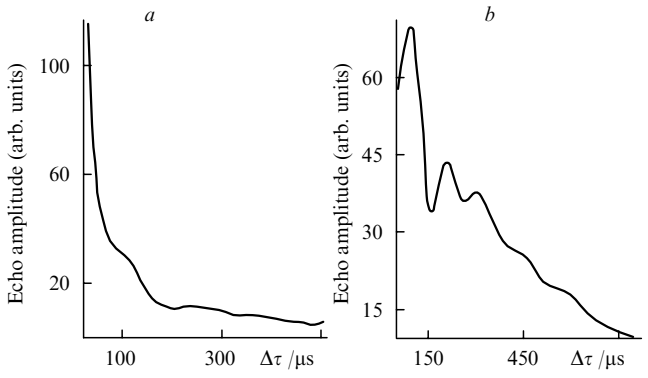


Figure 13. Zero-field spin echo envelopes of the ν_1 (*a*) and ν_2 (*b*) transitions in the ^{209}Bi NQR spectrum of powdered $BaBiO_2Cl$.

^{209}Bi NQR zero-field spectrum of a powder sample of $BaBiO_2Cl$ measured at 300 K is given below.

Transition frequency /MHz				eQq/h /MHz	η (%)
ν_1	ν_2	ν_3	ν_4		
33.43	36.44	57.50	77.67	470.25	33.3

Nearly all the compounds discussed here featured extraordinary sensitivity of the NQR spectroscopic parameters to weak magnetic fields. For most of them, a considerable increase in the resonance intensity depending on the ^{209}Bi EFG symmetry properties and mutual orientation of the fields disturbing the spin system was observed upon applying magnetic field (see, for instance, Figs 4 and 8). This phenomenon could explain the deviation of the ν_2Bi(1)-to-ν_2Bi(2) intensity ratio in $Bi_3B_5O_{12}$ from that in a pure quadrupole spectrum.[13]

A strong increase in the line intensity observed in the Zeeman spectrum of $Bi_4Ge_3O_{12}$ was suggested to result from the effect of external magnetic field on the spatial orientation of the EFG axes.[12] Recent experiments showed that $\boldsymbol{H}_e$ also strongly affects the spin–spin relaxation time and hence the resonance intensity (Fig. 14).[24] This problem for the high-spin systems with non-equidistant energy levels is, however, virtually unstudied.

It is important to note that no intensity increase in the ^{115}In NQR lines in a magnetic field was observed for crystallochemically related indium compounds In_xB_y (B = O, Se, Te) where the valence electron shell of the central atom (the ^{115}In nuclear spin is 9/2) has, unlike bismuth, no unshared pair of electrons (Table 4, Fig. 15).[24]

Table 4. The ^{115}In NQR spectrum of In_2Te at 77 K.

Atom	Transition frequencies /MHz				eQq/h /MHz	η (%)
	ν_1	ν_2	ν_3	ν_4		
In(1)	10.55	15.12	23.20	31.00	188.0	21.0
In(2)	8.06	10.46	16.37	22.00	133.0	25.0

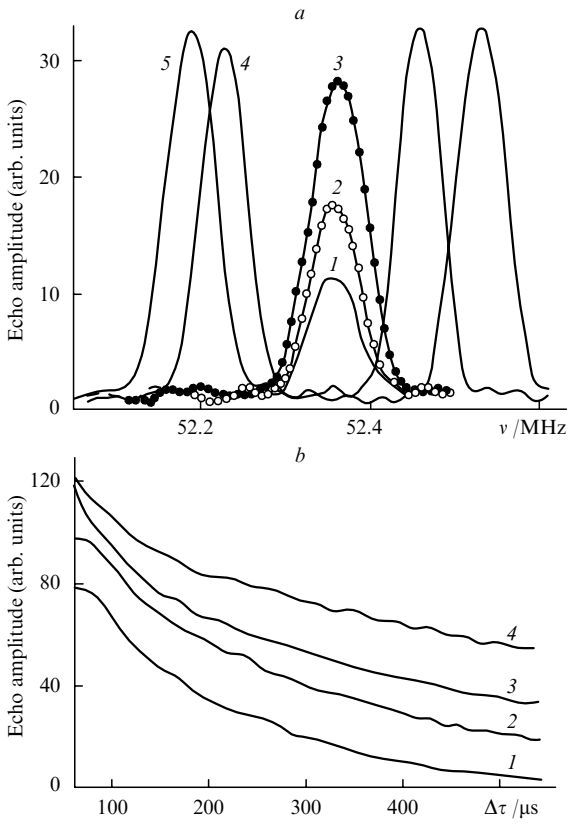


Figure 14. Line ofthe ν_2 transition of Bi(2) (see Table 2) in the ^{209}Bi NQR Zeeman spectra of $Bi_3B_5O_{12}$ (*a*) and spin-echo envelopes recorded for the same line in various magnetic fields (*b*).
H_e /Œ: (*a*) 0 (*1*), 13 (*2*), 30 (*3*), 225 (*4*), 300 (*5*); (*b*) 0 (*1*), 7.5 (*2*), 18 (*3*), 45 (*4*).

V. The results of magnetisation measurements and magnetoelectric effect in the α-Bi_2O_3 single crystal

Studies of magnetic properties of the compounds by complementary methods included an examination of a powdered α-Bi_2O_3 sample using a muon spin relaxation (μSR) technique[25–27] and SQUID measurements of the α-Bi_2O_3 single crystal.[28,29] The results of the experiments were understood as indicative of previously unknown magnetic properties in the compound. The μSR experiments within 10–300 K revealed no pronounced precession of the muon spin, hence ruling out the existence of a long-range order in α-Bi_2O_3. However, fast depolarisation of the muon spin was distinctly observed for short time intervals, which was interpreted as manifestation of local magnetic fields in interstices of the α-bismuth oxide crystal lattice.[25–27]

In the experiments using a SQUID magnetometer with the sensitivity of about 10^{-7} G cm^3, the magnetisation of the α-Bi_2O_3 single crystal was measured as a function of the magnetic field and temperature to find the paramagnetic character of magnetisation at low temperatures (~4.2 K) in magnetic fields up to 3–5 kŒ (Figs 16 and 17).[28] The magnetisation of the single crystal was highly anisotropic, which makes groundless a suggestion of paramagnetic impurities as the cause of magnetisation: because of disordered distribution in a diamagnetic crystal, they can produce the isotropic magnetisation only.[30]

As the temperature and external magnetic field increased, the magnetisation of α-Bi_2O_3 passed from the para- to the diamagnetic region where it conformed to the conventional classification of this substance as diamagnetic. It is to be noted that this classification is based on the results of measurements of the magnetisation by the Faraday method using a magnetic balance at room temperature in magnetic fields of the order of 10 kŒ.

A strong dependence of the α-Bi_2O_3 single crystal magnetisation (M) on the magnetic prehistory of the sample was observed.[29] Figure 18 demonstrates the $M(H)$ curves measured along the crystallographic c-axis of the sample at 4.2 K. The sample was cooled either in the zero external field (Zero-Field

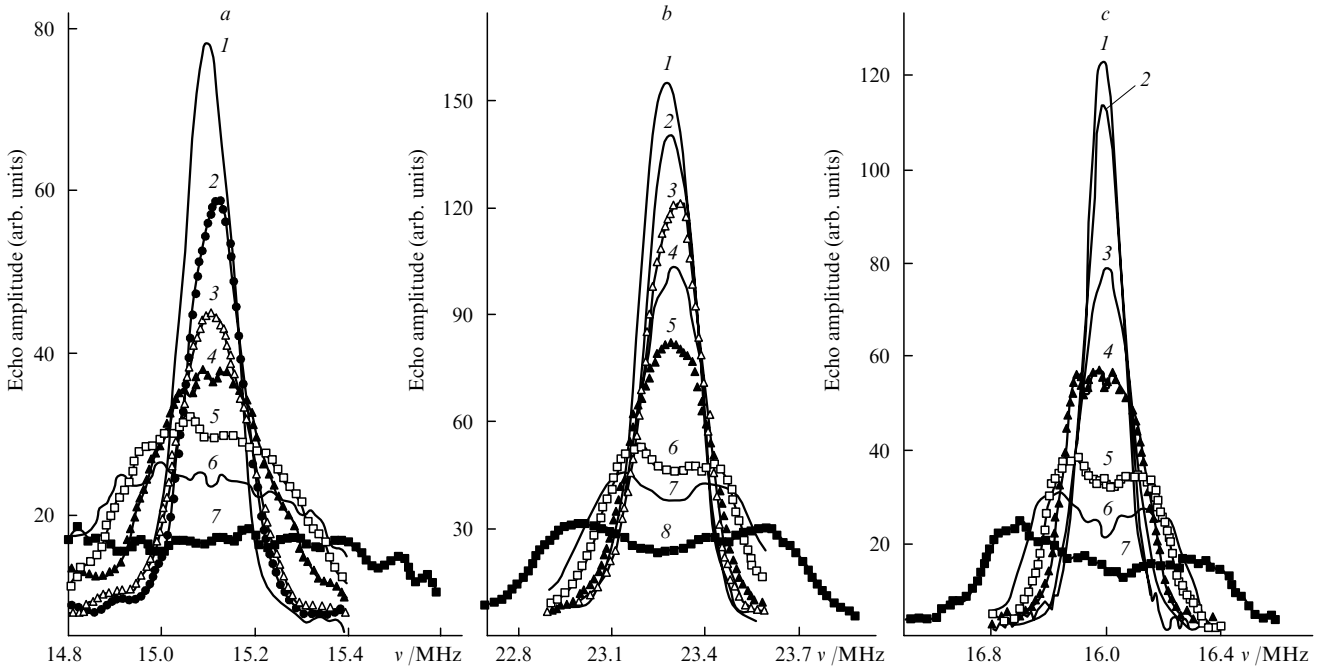


Figure 15. Selected lines assigned to the transitions ν_2 for In(1) (*a*), ν_3 for In(1) (*b*) and ν_3 for In(2) (*c*) in the ^{115}In NQR Zeeman spectra of powdered In_2Te (see Table 4).
H_e /Œ: (*a*) 0 (*1*), 21 (*2*), 60 (*3*), 150 (*4*), 225 (*5*), 300 (*6*), 480 (*7*); (*b*) 0 (*1*), 30 (*2*), 60 (*3*), 90 (*4*), 120 (*5*), 225 (*6*), 300 (*7*), 480 (*8*); (*c*) 0 (*1*), 30 (*2*), 90 (*3*), 150 (*4*), 225 (*5*), 300 (*6*), 480 (*7*).

Cooling, ZFC; the strength of H_e inside a magnetic screen containing the sample was several mŒ), or in the fields of the order of several hundred Oersted (Field Cooling, FC). The dependence $M(H)$ under the ZFC conditions was linear in weak fields and rapidly came to a saturation in the fields above 2.5 kŒ. However, the magnetisation dramatically increased upon cooling the crystal in the external magnetic field. Thus, it increased by an order of magnitude in the fields $H_e \sim 3-4$ kŒ for the sample precooled in the field of 580 Œ, the tendency for saturation weakening as the field in which the sample was cooled increased.[29]

The temperature dependence of the magnetisation also strongly depended on the magnetic prehistory of the sample.[29] Both curves in Fig. 19 were measured in the external filed of 4850 Œ applied along the axis *a* of the crystal. The curve *1* was measured after ZFC, whereas the other one, after the crystal was stored for ~10 hours in a residual field of a solenoid ($H_e \sim 10$ Œ) at liquid nitrogen temperature.

The mechanism of this phenomenon is not yet clear, the suggestion being made of its magnetoelectric nature, because the magnetoelectric effect (electric polarisation in an applied magnetic field) linear with respect to the field was observed in α-Bi_2O_3 at 4.2 K.[28,29] In addition, α-bismuth oxide is similar to ferro- and antiferroelectrics in electric properties. This is supported by

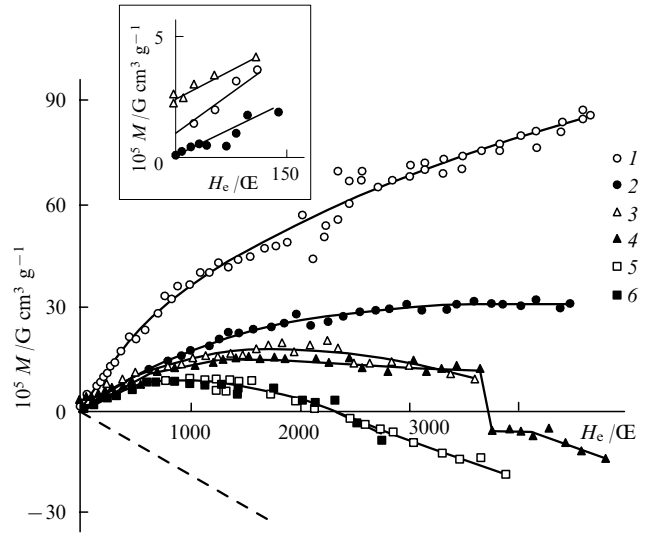


Figure 16. Magnetisation of the α-Bi_2O_3 single crystal in external magnetic fields.[28]
Measuring conditions: (*1*) $T = 4.2$ K, $\boldsymbol{H}_e \| a$; (*2*) $T = 4.2$ K, $\boldsymbol{H}_e \| b$; (*3*) $T = 4.2$ K, $\boldsymbol{H}_e \| c$; (*4*) $T = 77$ K, $\boldsymbol{H}_e \| a$; (*5*) $T = 77$ K, $\boldsymbol{H}_e \| c$; (*6*) $T = 200$ K, $\boldsymbol{H}_e \| c$.
Dashed line is M_{dia} (see text). In the inset, the initial parts of some curves are shown.

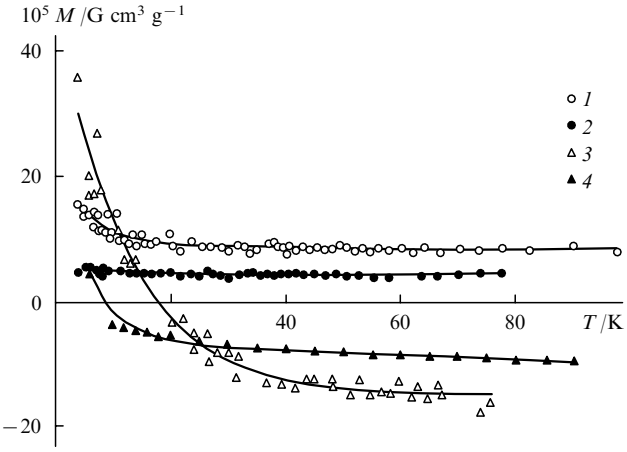


Figure 17. Temperature dependence of α-Bi_2O_3 magnetisation.[28]
Measuring conditions: (*1*) $\boldsymbol{H}_e \| c$, $H = 1000$ Œ; (*2*) $\boldsymbol{H}_e \| c$, $H = 124$ Œ; (*3*) $\boldsymbol{H}_e \| a$, $H = 4850$ Œ; (*4*) powder sample, $H = 500$ Œ.

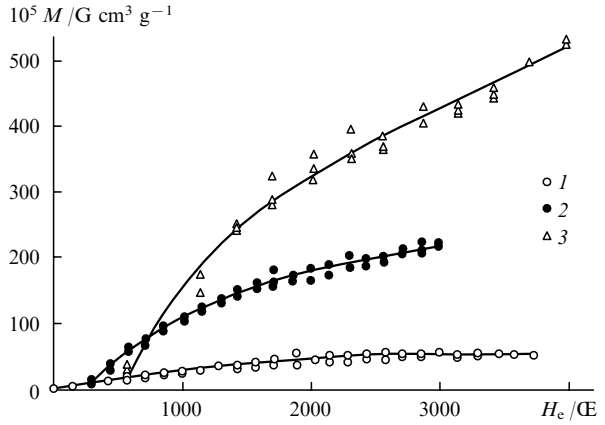


Figure 18. Field dependence of the α-Bi_2O_3 single crystal magnetisation measured at 4.2 K in $\boldsymbol{H}_e \,||\, c$.[29]
(*1*) ZFC, (*2*) FC in the field 284 Œ, (*3*) FC in the field 566 Œ.

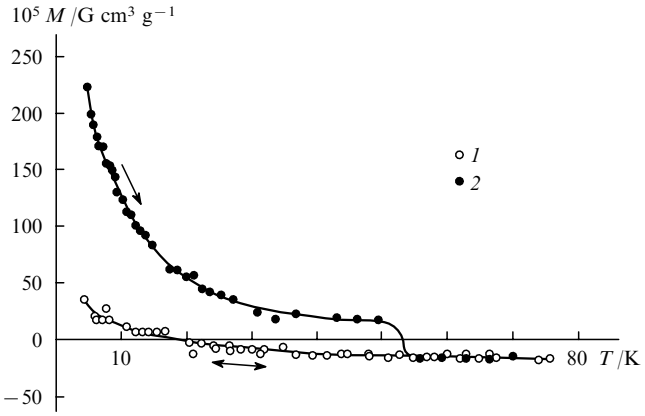


Figure 19. Temperature dependence of the α-Bi_2O_3 single crystal magnetisation measured in the field 4850 Œ, $\boldsymbol{H}_e \,||\, a$.[29] (*1*) ZFC, (*2*) a sample was stored in the field of 10 Œ at $T = 77$ K for 10 h. Arrows show the direction of temperature change.

several anomalies in its physical properties found between 450 – 570 K, for instance, a maximum displayed by the real part of the dielectric permeability.[31, 32] These anomalies were however accompanied by neither distortions of monoclinic symmetry of the α-Bi_2O_3 lattice, nor sharp changes in the lattice parameters over 300 – 570 K. The monoclinic lattice of α-bismuth oxide remained stable also at low temperatures: the IR[33] and Raman[34] spectra of the single crystal were qualitatively very similar to those measured at room temperature.

Based on the results of measurements of the field and temperature dependences of the α-Bi_2O_3 magnetisation, the authors[29] evaluated the effective magnetic moment per unit cell of the crystal, assuming several contributions to the magnetisation:

$$M = M_{\text{dia}} + M_{\text{VV}} + M_{\text{para}}, \tag{30}$$

where $M_{\text{dia}} = \chi_{\text{dia}} H$ is the temperature-independent diamagnetic contribution of the ionic cores (the magnitude of $\chi_{\text{dia}} = -1.85 \times 10^{-7}$ cm^3 g^{-1} was estimated assuming additive contributions of the ion diamagnetic susceptibilities to the total diamagnetic susceptibility of α-Bi_2O_3[35]); M_{VV} is the temperature-independent positive Van Vleck-type contribution; M_{para} is the paramagnetic Curie-type contribution. Both latter contributions depend on the magnetic prehistory of a sample (see Figs 18 and 19). The known formulae were used to evaluate M_{VV} and M_{para}:

$$\begin{aligned} M_{\text{VV}} &= \chi_{\text{VV}} H, \\ \chi_{\text{VV}} &\approx \frac{N_A \mu_B^2}{A} \frac{\alpha^2}{\Delta}, \\ M_{\text{para}} &= \chi_{\text{para}} H, \\ \chi_{\text{para}} &= \frac{N_A \mu_B^2}{A} \frac{\mu_{\text{ef}}^2}{3kT}, \end{aligned} \tag{31}$$

where N_A is the Avogadro number, $A = 466$ g mol^{-1} is the molecular weight of α-Bi_2O_3, α^2 is the squared matrix element of the magnetic moment operator, Δ is the energy difference between the ground and excited states of the electronic subsystem, μ_{ef} is the effective magnetic moment of the unit cell of the crystal.

The parameters α^2/Δ and μ_{ef} were estimated at 4.2 and 77 K based on the results of ZFC magnetisation measurements[28] (Figs 16 and 17) in weak fields ($H_e < 500$ Œ) where M linearly depends on $\boldsymbol{H}_e$ directed along the axis a of the crystal. They were found to amount to $\alpha^2/\Delta \approx 4 \times 10^{-4}$ K^{-1} and $\mu_{\text{ef}} \approx 0.06\ \mu_B$ (per formula unit). Although the estimated value of the α-Bi_2O_3 magnetic moment appeared to be small compared to those in conventional ferro- and antiferromagnets, it unambiguously points to the electronic origin of the paramagnetism in this compound. Moreover, the magnetisation of the sample precooled in a constant magnetic field (the FC experiment) increased by factors 5 – 10 compared to that of the sample measured after ZFC (see Fig. 18). It is clear that if Eqns (31) hold true under the FC conditions, a similar analysis of the magnetisation will give the values of α^2/Δ and μ_{ef} increased accordingly.

As was mentioned above, the magnetoelectric effect was observed in the α-Bi_2O_3 single crystal.[28, 29] This effect was studied for a plate ~ 0.03 cm^2 in area and 0.13 cm thick that was cut in the *bc* plane of the crystal. A highly sensitive electrometer Kythley 642 was used for the measurements. The experiment was carried out at 4.2 K in a superconducting solenoid capable of producing magnetic field up to 150 kŒ. The magnetic field $\boldsymbol{H} \,||\, \boldsymbol{E}$ was applied perpendicularly to the plate surface, *i.e.*, close to the axis a of the crystal. The results are shown in Fig. 20. As one can see, the polarisation linearly increased (the slope is 1.6×10^{-7}) in the fields up to 50 kŒ showing a tendency for saturation in higher fields.

The crystal structure of α-Bi_2O_3 is known to be monoclinic.[36] There are four magnetic classes in the point group C_{2h},[37] from which C_{2h} and $C_{2h}(C_i)$ allow ferromagnetism, whereas $C_{2h}(C_2)$ and $C_{2h}(C_s)$, antiferromagnetism. An inversion (I) is present among the symmetry elements of the two former classes. This means that the linear magnetoelectric effect described by the magnetoelectric component of the thermodynamic potential[37]

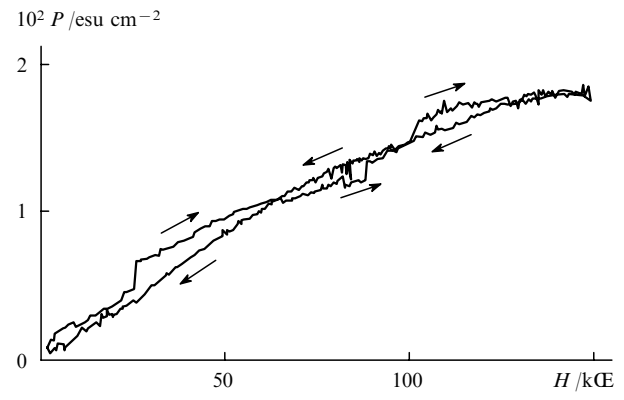


Figure 20. The magnetoelectric effect in the α-Bi_2O_3 single crystal measured at 4.2 K.[29]
P is polarisation. Arrows show the direction of field change.

$$\Phi_{\text{me}} = -\alpha_{ij} E_i H_j \tag{32}$$

is forbidden for the C_{2h} and $C_{2h}(C_i)$ classes (α_{ij} is the magnetoelectric tensor) and allowed for $C_{2h}(C_2)$ and $C_{2h}(C_s)$. Based on the symmetry properties, it was shown [29] that the magnetoelectric tensor for the class $C_{2h}(C_2)$ is

$$\alpha_{ij} = \begin{pmatrix} \alpha_{xx} & 0 & \alpha_{xz} \\ 0 & \alpha_{yy} & 0 \\ \alpha_{zx} & 0 & \alpha_{zz} \end{pmatrix}. \tag{33}$$

For the class $C_{2h}(C_s)$, the components complementary to those of matrix (33) differ from zero:

$$\alpha_{ij} = \begin{pmatrix} 0 & \alpha_{xy} & 0 \\ \alpha_{yx} & 0 & \alpha_{yz} \\ 0 & \alpha_{zy} & 0 \end{pmatrix}. \tag{34}$$

Attempts to explain the origin of the linear magnetoelectric effect in α-bismuth oxide faced however several difficulties.

According to Landau and Lifshitz, who predicted the existence of the effect in magnetically ordered substances,[37] the tensor α_{ij} is an odd function with respect to time inversion. After theoretical prediction by Dzyaloshinskii [38] followed by observation of the magnetoelectric effect in antiferromagnetic Cr_2O_3,[39,40] the systematic classification of magnetoelectric materials was performed.[41] It was noted that the linear magnetoelectric effect described by Eqn (32) can exist only in substances characterised by the long-range ferro- or antiferro-magnetic ordering. However, the analysis of the α-Bi_2O_3 magnetisation carried out using Eqn (30) showed that the existence of the long-range magnetic ordering in α-bismuth oxide is unlikely.[29]

The suggestion that the paramagnetoelectric effect, similar to that found in piezoelectric paramagnetic crystals,[42] may exist also in α-Bi_2O_3 comes into conflict with several facts. This effect is described by a contribution into the thermodynamic potential of the type

$$\Phi_{\text{PME}} = -\zeta_{ijk} E_i H_j H_k ,$$

where ζ_{ijk} is the magnetoelectric tensor of the third rank.

Hence, this is forbidden for the point group C_{2h}, because the inversion I is available among its symmetry elements. In addition, the electric polarisation is a function of H but not H^2 over a wide range of fields, as demonstrated in Fig. 20.

As to the existence of the magnetoelectric effect in diamagnetic dielectric crystals, the observation of this effect in crystals with paramagnetic defects was documented. Using EPR, a notable increase in magnetisation of α-quartz comprising the $Al-O^-$ centres was found in an alternating electric field.[43] The magnetic and electric characteristics are coupled in such systems by spin–orbit interaction. A tunnelling of the charged electron holes between the equilibrium positions, if available, enhances the effect considerably. The hole is known to carry the magnetic moment because it possesses both spin and orbital magnetic moments. Such a paramagnetic centre carries also the electric dipole moment. If a coupling exists between the electric and magnetic moment, one can observe the magnetoelectric effect.

The existence of a system of paramagnetic centres in α-Bi_2O_3 is quite probable. The holes in the p-electron shell of the oxygen atoms may presumably serve as such centres, whereas the $Al-O^-$ centres in α-quartz result from the Al^{3+} substitution for Si^{4+}. Considering the low symmetry of the electric field of the crystal at the oxygen sites and weak spin–orbit interaction (the spin–orbit coupling constant for the oxygen atom is ~ 10 meV) one can admit the presence of several low-lying crystal field levels, which are responsible for the observed field and temperature dependences of the paramagnetic contribution into the α-Bi_2O_3 magnetisation. Thus for the p^4 atomic configuration, the multiplets $^3P_2$ (ground) and excited $^3P_1$ and $^3P_0$ (lying, accordingly, 20 and 30 meV above the ground level in a free oxygen atom [44]) must split into nine crystal-field levels. To verify the hypothesis for the presence of the paramagnetic centres in α-bismuth oxide, a detailed examination of its electron structure is necessary.

VI. On the probable origin of anomalies in magnetic properties of bismuth oxy compounds

No information on the electron structure of α-Bi_2O_3 is available in the literature, so that the calculation of its electron band structure was found to be expedient. The program package used for the calculations was a version of the FP-LMTO (Full-Potential Linear-Muffin-Tin-Orbital) approach [45] based on the electron density functional theory.[46] This approach belongs to the so-called 'first principle' methods of calculating the electron structure, which require only the nuclear charges, lattice parameters and atomic coordinates to be given as the initials. Based on the electron density functional theory, the electron density is further computed by a self-consistence procedure, after which the full energy and electron band structure of the compound are evaluated. The calculated electron band structure of α-Bi_2O_3 appeared however too cumbersome, therefore the density of states only is shown in Fig. 21, which nevertheless carries a sufficient amount of information on the electronic properties of this compound.

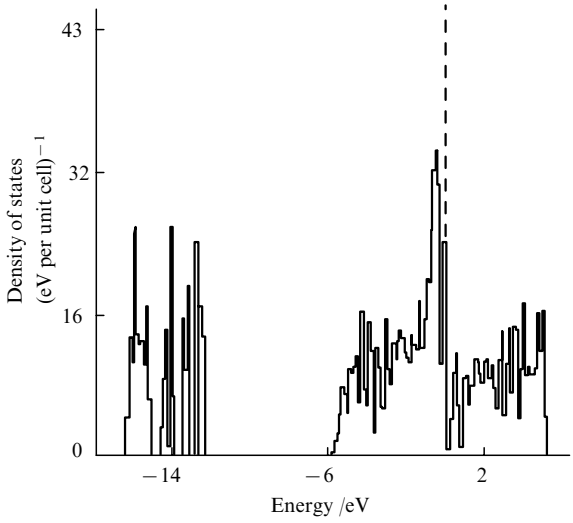


Figure 21. Density of states for α-Bi_2O_3. Dashed line shows the Fermi level.

According to the results of the calculation, a peak of the density of states exists near the Fermi level, the ground state of the electron structure of α-Bi_2O_3 being metallic, whereas it is actually dielectric. A similar inconsistence results from the electron structure calculations of copper oxy compounds that served as the initial reagents for the preparation of high-temperature superconductors. This inconsistence can be removed, for instance, by the introduction of the Hubbard Hamiltonian, which takes into account the electron correlations. Examples are provided by transition or rare earth element compounds that exhibit sharp peaks of the density of states near the Fermi surface (Kondo-insulators).[47] Unlike the known systems with strong electron correlations, α-Bi_2O_3 comprises no atoms with unfilled d- or f-electron shells. Hence, the revealed features of the α-Bi_2O_3 electron structure allow one to raise the question about the existence of strong electron correlations in systems with valence s- and p-electrons also.

The analysis of the partial densities of states suggested that the Bi6s- and O2s-electrons make the predominant contribution to the peaks located in the energy range from −16 to −12 eV, the high density of states at −5.0 and −3.0 eV resulting largely from

the Bi6p- and O2p-electrons. The unoccupied states above the Fermi level are due mostly to the Bi6p-electronic states. Based on the results of the calculations, the conduction band width ($\sim 4-5$ eV) involving the hybridised O2p- and Bi6p-electronic states was evaluated as well as the band width for the O2p-states in the Fermi level (2 – 3 eV). As follows from the results obtained, the correlations between the O2p-electrons may be responsible for the semiconducting (close to dielectric) type of the α-Bi_2O_3 electron band structure as well as for the unusual magnetic properties: the existence of local magnetic fields, paramagnetism depending on the thermomagnetic prehistory of a sample and magnetoelectric effect. The Bi6s- and O2s-electronic states in α-bismuth oxide can hardly be the strongly correlated subsystem, if the high bonding energy and the Pauli principle are taken into account. The dominant role played by the Bi6p-electrons seems to be the participation in the superexchange O2p – Bi6p – O2p interactions accompanied with the electron spin-flip hoppings, which may result in the antiferromagnetic correlations and magnetoelectric effect.[48] This suggestion is supported by low (monoclinic) crystal symmetry of α-bismuth oxide removing the spin – orbit degeneracy of the 6p-electron levels, a gain in energy caused by the half-filled bismuth 6p-electron shell (the $6s^26p^3$ configuration), and high, as the calculation showed, density of the vacant 6p-states above the Fermi level. It is to be noted that the ferromagnetic correlations in systems comprising only p-electrons are forbidden by the Pauli principle.

VII. Conclusion

This review summarises the results of investigation of some unusual magnetic and electronic properties of bismuth oxy compounds comprising the Main Group elements only. The results were obtained using mainly the ^{209}Bi NQR spectroscopy and SQUID-magnetometry. The quantitative analysis of both the complicated Zeeman NQR spectra of high multiplicity and quadrupole spin echo envelopes, measured on mono- and polycrystalline samples, became possible due to development of new approaches in the NQR theory, *viz*., elaboration of the computer model of the quadrupole spin echo based on the density matrix formalism and account of the EFG symmetry properties. As a result, the high sensitivity of the NQR spectroscopy to the presence in substances of weak magnetic fields compared to the terrestrial field was demonstrated. Because of this superior sensitivity, the NQR method (along with NMR) may become a promising tool for the solution of topical problems concerned with the reading of an information stored by nuclear spin systems.

A variety of unusual magnetic properties revealed in the bismuth oxy compounds, which have been traditionally considered as diamagnets, namely,

— the existence of local magnetic fields,

— the paramagnetism depending on the magnetic prehistory of a sample,

— magnetoelectric effect linear in magnetic field

give, along with the calculated peaks of the density states near the Fermi surface, grounds to believe that the electron correlations may exist also in substances with valence s- and p-electrons.

The electronic and magnetic properties of the discussed bismuth oxy compounds, as well as those of extensively studied transition and rare earth element oxides, result from an interplay of a number of contributions, such as specific features of crystal structure, electron correlations, exchange and superexchange interactions and orbital degrees of freedom.

An extension and analysis of the experimental basis aimed at clarifying the origin and mechanism of the coupling between the electronic and magnetic subsystems in non-magnetic compounds make a valuable contribution to our knowledge of magnetism. Thus the material surveyed in this review suggests the important role of the matrix (of gallium arsenide-type) for the explanation of unconventional properties displayed by highly dilute magnetic semiconductors recognised as promising materials for spintronics technology.

The authors are grateful to the Russian Foundation for Basic Research (Project No. 02-03-33280) for the support. The authors also appreciate the support of The Department of Chemistry and Materials Sciences of the RAS (the program 'Elaboration of new efficient methods of chemical analysis and srtructural studies of substances and materials', Project OKh-2.14) (E A Kravchenko); Federal Program for the Support of Leading Scientific Schools of the Russian Federation (Grant NSh-15722.2003.2) and The Foundation for the support of basic research in RSC 'Kurchatov Institute' (Project No. 17) (V G Orlov and M P Shlykov).

VIII. Appendix. The calculation of the nuclear quadrupole spin echo

The numerical modelling of the quadrupole spin echo was carried out for a two pulse spin echo sequence. The radiofrequency field H_{rf} was supposed to act during the time intervals $0 \leqslant t \leqslant t_1$ (the first pulse) and $\tau \leqslant t \leqslant \tau + t_2$ (the second pulse) and be switched off between the pulses ($t_1 \leqslant t \leqslant \tau$) and after the second pulse ($t \geqslant \tau + t_2$). The spin echo signal was expected to appear at the moment $t \cong 2\tau$. The duration of both pulses was assumed to be short compared to the interval between the pulses (t_1, $t_2 \ll \tau$). The interval τ is usually restricted to $\tau < T_2$ where T_2 is the spin – spin (transverse) relaxation time. In the modelling of the spin echo envelope, the magnitude of τ was varied in consistence with the time of measuring the SEE.

A distinctive feature of this model of the quadrupole spin echo consists of the presence of local and external magnetic fields. Both fields were assumed to be small: γH_{loc}, $\gamma H_e \ll \omega_Q$, where $\gamma/2\pi = g_{Bi}\mu_B/h = 6.9 \times 10^{-4}$ MHz (G^{-1}) is the gyromagnetic ratio for the bismuth nucleus, ω_Q is the quadrupole transition frequency. The radiofrequency field H_{rf} was also assumed to be small: $\omega_1 = \gamma H_{rf} \ll \omega_Q$.

In the NQR experiments on the bismuth oxy compounds, the magnetic fields do fulfil the above requirements. Thus in the ^{209}Bi NQR spectrum of $Bi_2Ge_3O_9$, the frequency ω_Q of transition between the nuclear spin levels $1/2 \rightarrow 3/2$ is ~ 160 MHz, the quadrupole coupling constant eQq_{zz}/h amounting to 605.9 MHz. One can easily find that the magnetic field strength H, derived from the relationship $\gamma H \sim \omega_Q$, is of the order of $(3-4) \times 10^4$ G, which is much larger than the local magnetic fields detected using NQR in the bismuth oxy compounds (30 – 250 G). In the NQR Zeeman experiments discussed here, the external magnetic fields up to 500 Œ were applied. The strength of H_{rf} in the coils of pulse NQR spectrometers also did not exceed several hundred Oersted, because the spin echo signal is observed if $\omega_1 t_{1,2} \sim 1$, the radiofrequency pulse widths $t_{1,2}$ being of the order of 1 – 10 μs. Under the optimum observation conditions, the spin echo frequency ω_1 must be of the order of 1×10^6 s^{-1}, which gives $H_{rf} \sim 200$ G. In addition, the condition $\omega_Q t_{1,2} \gg 1$ is also satisfied.

In order to observe the nuclear quadrupole resonance signal, one has not to place a sample in a constant external magnetic field, because the nuclear spin levels are split due to the interaction of the nuclear electric quadrupole moment with a non-uniform electric field inherent in the sample. The level spacing can be found by the calculation of the energy levels of the quadrupole Hamiltonian. In the system of the EFG principal axes (x', y', z'), the quadrupole Hamiltonian is

$$\hat{H}_Q = \frac{eQq_{zz}}{4I(2I-1)}\left[3I_{z'}^2 - I(I+1) + \frac{\eta}{2}(I_+^2 + I_-^2)\right], \qquad \text{(A.1)}$$

where $I_\pm = I_{x'} \pm iI_{y'}$.

In the presence of external and local magnetic fields, the term describing the interaction of the nuclear magnetic moment with these fields should be added to Eqn (A.1) to give the time-independent Hamiltonian

$$\hat{H}_0 = \hat{H}_Q - \gamma\hbar\boldsymbol{H}_{\rm loc}\hat{\boldsymbol{I}} - \gamma\hbar\boldsymbol{H}_{\rm e}\hat{\boldsymbol{I}}. \tag{A.2}$$

The interaction of the nuclear magnetic moment with radiofrequency field $\boldsymbol{H}_{\rm rf}$ is described as follows:

$$\hat{H}_1 = -\gamma\hbar\ 2\boldsymbol{H}_{\rm rf}\hat{\boldsymbol{I}}\cos\omega t. \tag{A.3}$$

The total Hamiltonian is the sum of the Hamiltonians (A.2) and (A.3):

$$\hat{H} = \hat{H}_0 + \hat{H}_1\,. \tag{A.4}$$

Under the action of pulsed radiofrequency field, the nuclear spin operators will evolve in time, so it is convenient to model the quadrupole spin echo using the time dependent density matrix [20, 49] with the elements

$$\rho_{mm'} = (m|\rho|m'), \tag{A.5}$$

where m, m' are the state numbers. The time dependence of ρ can be found from the Liuville quantum equation (the Neumann equation) [49]

$$\mathrm{i}\hbar\frac{\partial\rho}{\partial t} = \left[\hat{H},\rho\right] = \hat{H}\rho - \rho\hat{H}, \tag{A.6}$$

where $\hat{H}$ is the total Hamiltonian (A.4).

Thus, the calculation of the quadrupole spin echo deals with the response of the nuclear spin system described by the Hamiltonian (A.2), the Hamiltonian (A.3) being taken into account.

At the initial moment, the density matrix $\rho(0)$ is given by the normalised Boltzmann distribution

$$\rho(0) = \frac{N}{2I+1}\exp\left(-\frac{H_0}{kT}\right), \tag{A.7}$$

where N is the number of nuclei in a sample. In the high-temperature approximation ($eQq_{zz} \ll kT$) this formula becomes

$$\rho(0) \approx \frac{N}{2I+1}\left(1-\frac{H_0}{kT}\right). \tag{A.8}$$

The solution of Eqn (A.6) using an evolution operator S [49] is described as follows:

$$\rho(t) = S\rho(0)S^{-1}. \tag{A.9}$$

The evolution operator S obeys the Schrödinger equation, the unit matrix E satisfying the initial condition

$$\mathrm{i}\hbar\frac{\partial S}{\partial t} = \hat{H}S, \text{ at } S(0) = E. \tag{A.10}$$

In the earlier publications on the quadrupole spin echo theory that made use of the density matrix formalism (see, for instance, Ref. 20), the evolution operator S was used as the product of transformation matrices R and D, referring, respectively, to the duration of the radiofrequecny field action and intervals between the pulses:

$$S = D_nR_n\ldots D_2R_2D_1R_1\,. \tag{A.11}$$

Here

$$D_n(t,t_{n0}+t_n) = \exp\left[-\left(\frac{\mathrm{i}}{\hbar}\right)H_0(t-t_{n0}-t_n)\right]$$

is the solution of the Schrödinger equation in the interval between the nth and $(n+1)$th pulses ($H_1 = 0$); $R_n(t,t_{n0})$ is the solution of the Schrödinger equation at the moment t of the nth pulse duration ($t_{n0} \leqslant t \leqslant t_{n0} + t_n$)

$$\mathrm{i}\hbar\frac{\partial R_n(t,t_{n0})}{\partial t} = (H_0+H_1)R_n(t,t_{n0}), \tag{A.12}$$

where t_{n0} is the time of switching the nth pulse on and t_n is its duration (the first pulse is assumed to be switched on at the moment $t_{10} = 0$).

The Schrödinger equation was solved with the unit matrix E satisfying the initial condition for all the matrices R and D in (A.11) (see Ref. 20). Using the interaction representation,[49] Eqn (A.12) can be rewritten as follows:

$$\begin{aligned} &R_n(t,t_{n0}) = \exp\left[-\frac{\mathrm{i}}{\hbar}H_0(t-t_{n0})\right]\tilde{R}_n(t,t_{n0}),\\ &\mathrm{i}\hbar\frac{\partial\tilde{R}_n}{\partial t} = \tilde{H}_1\tilde{R}_n\,, \end{aligned} \tag{A.13}$$

where

$$\tilde{H}_1(t) = \exp\left[\frac{\mathrm{i}}{\hbar}H_0(t-t_{n0})\right]H_1(t)\ \exp\left[-\frac{\mathrm{i}}{\hbar}H_0(t-t_{n0})\right].$$

The solution of (A.13) was given in Ref. 20 as

$$\tilde{R}_n(t,t_{n0}) = \exp\left[-\frac{\mathrm{i}}{\hbar}\int_{t_{n0}}^{t}\tilde{H}_1(t')\mathrm{d}t'\right]. \tag{A.14}$$

Formula (A.14) as well as the presentation of the evolution matrix as a chain of products of matrices $S = D_nR_n\ \ldots\ D_2R_2D_1R_1\,$, each being a solution of the Schrödinger equation with the unit matrix E satisfying the initial condition, are valid, provided the Hamiltonian $\tilde{H}_1(t)$ in (A.13) is independent of time. Since in the latter case $\tilde{H}_1(t)$ is a function of time, the procedure of finding S should be modified, the changes concerning the calculation of matrices $R_n(t,t_{n0})$. Generally, when the condition $\omega_{\rm Q}t_{1,2} \gg 1$ is ignored and magnetic fields are not small, these matrices can be found by Eqn (A.13). Upon solving this equation, it is not E that should be taken to satisfy the initial condition but rather the evolution matrix value at the preceding stage $D_{n-1}R_{n-1}\,$.

As before, the matrix D_n in the interval between the nth and $(n+1)$th pulses may be presented in the form

$$D_n(t,t_{n0}+t_n) = \exp\left[-\frac{\mathrm{i}}{\hbar}H_0(t-t_{n0}-t_n)\right],$$

which follows from the solution of the Schrödinger equation, the unit matrix E satisfying the initial condition. In this case, the evolution matrix at the moment of switching the $(n+1)$th pulse on is calculated by multiplying the matrices $S = D_nR_n$. For instance, the procedure of calculating the evolution matrix for the two-pulse method of spin echo registration may be presented as follows:

$$S(t,0) = D_2(t,\tau+t_2)\,R_2(\tau+t_2,\tau)\Big|_{D_1(\tau,t_1)\,R_1(t_1,0)}\Big|_E \tag{A.15}$$

A shorthand notation was introduced in order to avoid a cumbersome description of the initial conditions:

$$S = D_2R_2\ \times\ D_1R_1, \tag{A.16}$$

where $\times$ denotes a procedure of calculating matrix R_2, the initial condition being D_1R_1. A multipulse chain can be presented similarly:

$$S = D_nR_n \times D_{n-1}R_{n-1} \times\ \ldots\ \times D_2R_2 \times D_1R_1\,, \tag{A.17}$$

where $\times$ denotes the operation specified by Eqns (A.15) and (A.16).

One can show that equation (A.17) is transformed to (A.11), which was used in the earlier publications on the quadrupole spin echo theory,[20] if, along with the above mentioned conditions ($\gamma H_{\rm e} \ll \omega_{\rm Q}$, $\gamma H_{\rm loc} \ll \omega_{\rm Q}$, $\omega_{\rm Q}t_{1,2} \gg 1$), the following condition is also satisfied:

$$\gamma H_{\rm e,\,loc}\,t_{1,2} \ll 1. \tag{A.18}$$

The condition (A.18) imposes the restriction $H_{\rm e,\,loc} \ll 200$ Œ on the external (or local) magnetic field strength in the bismuth

compounds. If Eqn (A.18) holds true, Eqn (A.13) for the matrix $\tilde{R}_n$ is reduced to

$$\frac{\partial \tilde{R}_n}{\partial t} = A\tilde{R}_n\,, \tag{A.19}$$

where A is a time-independent matrix. An explicit expression for the matrix $\tilde{R}_n$ can further be found by a cumbersome computation. If the condition (A.18) is not satisfied, the matrix $\tilde{R}_n$ can be found by a numerical solution of Eqn (A.13).

Assuming the condition (A.18) is satisfied and Eqn (A.11) holds true, one can derive the formula for the average value of nuclear spin projection onto the rf-coil axis $\langle I\rangle$, and use it as the basic formula for further elaborating a scheme of modelling of the SEE in $H_{\mathrm{e,loc}} \ll 200$ Œ (the latter restriction was undoubtedly satisfied in the experiments discussed). If the time dependence of $\langle I\rangle$ is known, one can find a derivative $\mathrm{d}\langle M\rangle/\mathrm{dt}$ of the nuclear magnetic moment projection ($\langle M\rangle = g_{\mathrm{Bi}}\mu_{\mathrm{B}} < \langle I\rangle$), to which the intensity of the spin echo signal is proportional.

According to the density matrix formalism, the average spin of a nuclear subsystem is evaluated by the formula

$$\langle I\rangle = \mathrm{Sp}(\rho\hat{I}). \tag{A.20}$$

In the high-temperature approximation, the density matrix at the initial moment is determined by formula (A.8). At any subsequent moment, the value of the matrix can be found by Eqn (A.9). Since $\mathrm{Sp}(\hat{I}) = 0$, the expression for the average moment is

$$\langle I\rangle = C\ \mathrm{Sp}\big(SH_0S^{-1}I\big), \tag{A.21}$$

where

$$C = -\frac{N}{(2I+1)kT}.$$

Using Eqn (A.11) for the evolution operator S, one can derive an expression for calculating the average nuclear spin after the action of the first

$$\langle I\rangle = C\ \mathrm{Sp}\big(D_1R_1H_0R_1^{-1}D_1^{-1}I\big) \tag{A.22}$$

and second

$$\langle I\rangle = C\ \mathrm{Sp}\big(D_2R_2D_1R_1H_0R_1^{-1}D_1^{-1}R_2^{-1}D_2^{-1}I\big) \tag{A.23}$$

readiofrequency pulses.

Substituting D_1 and D_2 into Eqns (A.22) and (A.23) and using the interaction representation, one obtains

$$\langle I\rangle = C\ \mathrm{Sp}\left[\left(-\frac{\mathrm{i}}{\hbar}H_0t\right)\ \tilde{R}_1H_0\tilde{R}_1^{-1}\exp\left(\frac{\mathrm{i}}{\hbar}H_0t\right)\ I\right], \tag{A.24}$$

$$\langle I\rangle = C\ \mathrm{Sp}\left[\exp\left(-\frac{\mathrm{i}}{\hbar}H_0(t-\tau)\right)\times\right. \tag{A.25}$$

$$\times\ \tilde{R}_2\exp\left(-\frac{\mathrm{i}}{\hbar}H_0\tau\right)\ \tilde{R}_1H_0\tilde{R}_1^{-1}\exp\left(\frac{\mathrm{i}}{\hbar}H_0\tau\right)\tilde{R}_2^{-1}\ \times$$

$$\left.\times\ \exp\left(\frac{\mathrm{i}}{\hbar}H_0(t-\tau)\right)\ I\right].$$

Using further the representation of operators in the basis of eigenfunctions for the operator $\hat{H}_0$ (A.2) and denoting $\omega_{ij} = \lambda_i - \lambda_j$ (where $\lambda_i = E_i/\hbar$ and E_i are the eigenvalues of the Hamiltonian $\hat{H}_0$), one can derive the expressions for calculating the average nuclear spin at instants after the first [formula (A.26)] and second [formula (A.28)] radiofrequency pulses

$$\langle I\rangle = C\sum_{m,s} A_{ms}(t)I_{sm}\,, \tag{A.26}$$

where

$$A_{ms}(t) = \mathrm{e}^{\mathrm{i}\omega sm t}\sum_n \lambda_n\big(\tilde{R}_1\big)_{mn}\big(\tilde{R}_1^*\big)_{sn}\,, \tag{A.27}$$

$$\langle I\rangle = C\sum_{m,s} B_{ms}(t,\tau)I_{sm}\,, \tag{A.28}$$

$$B_{ms}(t,\tau) = \sum_{n,k,p}\left\{\exp \mathrm{i}\omega_{sm}\left[t-\left(1+\frac{\omega_{np}}{\omega_{sm}}\right)\tau\right]\right\}\times \tag{A.29}$$

$$\times\ \lambda_k\big(\tilde{R}_2\big)_{mn}\big(\tilde{R}_1\big)_{nk}\big(\tilde{R}_1^*\big)_{pk}\big(\tilde{R}_2^*\big)_{sp}\,.$$

Since the operator $\hat{I}$ is Hermitian and the eigenfunctions of the Hamiltonian $\hat{H}_0$ are real, the following relationships hold true: $A_{sm}^* = A_{ms}$, $B_{sm}^* = B_{ms}$. As a result, the average spin values calculated by formulae (A.26) and (A.28) are real.

The formula (A.29) clearly indicates when the spin echo signal appears. It is important that the Hamiltonian (A.2), which determines the scale of energy levels spacing [in this case, the quadrupole Hamiltonian (A.1)], be independent of time in the absence of radiofrequency field. The spin echo signal appears at the instants

$$t = \left(1+\frac{\omega_{np}}{\omega_{sm}}\right)\tau,$$

defined by the ratio of various frequencies in the Hamiltonian (A.2) Among them, the spin echo appearing at the moment $t = 2\tau$ is always present. The signal intensity is determined by coefficients B_{ms} (A.29), which reach their maxima when the frequency of H_{rf} is close to the frequencies ω_{sm} and ω_{np}.

The free induction decay signals appearing after the first and second pulses ($t = t_1$ and $t = \tau + t_2$) can also be modelled using expression (A.28). As formulae (A.28) and (A.29) show, one can observe the spin echo signals for nuclei with spin $I > 3/2$ not only at the moment 2τ, but, for instance, also at $t = 3\tau$. For nuclei with spin $I = 3/2$, the spin echo is observed at $t = 2\tau$ solely, because only one quadrupole transition frequency is available. Whether the spin echo at $t = 3\tau$ is observable, depends on the signal intensity, which is defined by Eqn (A.29).

Formulae (A.26) and (A.28) can be conveniently used for calculating the average nuclear spin in an external magnetic field. Upon varying a pulse separation τ [see Eqns (A.28) and (A.29)] in the presence of static external or local magnetic fields, one can observe modulations (beats) on the SEE curve.[20] Their frequencies are proportional to the Zeeman-perturbed splittings of the nuclear spin levels described by the Hamiltonian (A.2). For the calculation of SEE, the absolute maximum of expression (A.29) at $t \sim 2\tau$ should be found for each τ.

Since the relaxation effects (a decay of the spin echo signal) were ignored in the Hamiltonian (A.4), on simulation they can be incorporated by simple multiplying the spin echo amplitude by a factor $\exp[-(1/2T_2^2)\tau^2]$, the value of T_2 being taken from the experiment.

The procedure of modelling the quadrupole spin echo signals should also take account of a mutual orientation of the laboratory $(\tilde{x},\tilde{y},\tilde{z})$ and crystallographic (x,y,z) coordinate systems. The appropriate relationships involve the Euler angles α, β and γ. The system of the EFG principal axes (x',y',z') is related to the crystallographic system by another set of the Euler angles θ, φ and ψ. The orientation of the local magnetic field vector $\boldsymbol{H}_{\mathrm{loc}}$ with respect to the EFG principal axes is determined by angles θ_{loc} and φ_{loc}. Thus, the direction of the fields $\boldsymbol{H}_{\mathrm{e}}$, $\boldsymbol{H}_{\mathrm{loc}}$ and $\boldsymbol{H}_{\mathrm{rf}}$ with respect to the principal axes system (x',y',z') of the quadrupole Hamiltonian (A.2) is completely determined by the angles $\alpha,\beta,\gamma,\theta,\varphi,\psi$, θ_{loc} and φ_{loc}. All the scalar products $\boldsymbol{H}_{\mathrm{e}}\boldsymbol{I}$, $\boldsymbol{H}_{\mathrm{loc}}\boldsymbol{I}$ and $\boldsymbol{H}_{\mathrm{rf}}\boldsymbol{I}$ in the Hamiltonians (A.2) and (A.3) have to be determined in the same coordinate system. For this purpose, the matrix D determined by angles θ, φ, ψ, α, β and γ, which projects the vectors $\boldsymbol{H}_{\mathrm{e}}$ and $\boldsymbol{H}_{\mathrm{rf}}$

onto the EFG principal axes, is involved into the calculation scheme. The crystallographically equivalent bismuth sites may appear to be magnetically non-equivalent. In such a case, each type of the EFG tensors is specified in external magnetic field by its own principal axes system (see Section III), so that the average nuclear spin is calculated for each orientation of the EFG tensors. The net average spin of the nuclear subsystem will evidently be the sum of the contributions from all the magnetically nonequivalent EFG tensors.

For a polycrystalline (powdered) specimen, the calculation procedure is similar. It differs in that the calculated spin is averaged over all the orientations of the crystallites with respect to the laboratory system, *i.e.*, over the Euler angles α, β and γ.

Thus, the procedure of calculation of the spin-echo amplitude as a function of radiofrequency pulse separation τ in weak ($\ll 200$ Œ) magnetic field involves the following stages:

1) the analysis of the EFG tensor symmetry; the evaluation of the matrix D: the calculation is performed for each magnetically non-equivalent EFG tensor;

2) the calculation of the eigenvalues and eigenfunctions of the Hamiltonian $\hat{H}_0$ (see A.2);

3) the calculation of matrix elements for operators using the representation in the eigenfunctions basis of the operator $\hat{H}_0$;

4) the evaluation of the matrix $\tilde{R}$ with the unit initial condition by solving the Schrödinger equation (A.13);

5) the computation of coefficients A_{ms} and B_{ms} in equations (A.27) and (A.29);

6) the evaluation of the absolute maximum of expression (A.29);

7) the incorporation of the spin echo relaxation effect by multiplying by a factor $\exp[-(1/2T_2^2)\tau^2]$.

References

1. E A Kravchenko, V G Orlov *Z. Naturforsch. A: Phys. Sci.* **49** 418 (1994)
2. N E Ainbinder, G A Volgina, E A Kravchenko, A N Osipenko, A A Gippius, Fam Suan Hai, A A Bush *Z. Naturforsch. A: Phys. Sci.* **49** 425 (1994)
3. E A Kravchenko, Fam Suan Khai, Yu F Kargin *Neorg. Mater.* **33** 1001 (1997) [a]
4. E A Kravchenko, V G Orlov, Fam Suan Hai, Yu F Kargin *Z. Naturforsch. A: Phys. Sci.* **53** 504 (1998)
5. Yu A Buslaev, E A Kravchenko, L Kolditz *Coord. Chem. Rev.* **82** 1 (1987)
6. Yu A Buslaev, E A Kravchenko, M Yu Burtzev, L A Aslanov *Coord. Chem. Rev.* **93** 185 (1989)
7. V G Orlov *J. Magn. Magn. Mater.* **61** 337 (1986)
8. P T Das, E L Hahn *Nuclear Quadrupole Resonance Spectroscopy* (New York, London: Academic Press, 1958)
9. N Niizeki, M Wachi *Z. Kristallogr.* **127** 173 (1968)
10. S F Radaev, L A Muradyan, Yu F Kargin, V A Sarin, V N Kanepit, V I Simonov *Kristallografiya* **35** 361 (1990) [b]
11. B C Grabmaier, S Haussühl, P Klüfers *Z. Kristallogr.* **149** 261 (1979)
12. E A Kravchenko, Yu F Kargin, V G Orlov, T Okuda, K Yamada *J. Magn. Magn. Mater.* **224** (3) 249 (2001)
13. E A Kravchenko, V G Morgunov, Yu F Kargin, A V Egorysheva, V G Orlov, M P Shlikov *Appl. Magn. Res.* **27** (1–2) 65 (2004)
14. V G Orlov, E A Kravchenko *Physica B: Condens. Matter* **259–261** 564 (1999)
15. E A Kravchenko, V G Orlov *Physica B: Condens. Matter* **312–313** 772 (2002)
16. A Vegas, F H Cano, S Garsia-Blanco *J. Solid State Chem.* **17** 151 (1976)
17. S Filatov, Yu Shepelev, R Bubnova, N Sennova, A V Egorysheva, Yu F Kargin *J. Solid State Chem.* **177** 515 (2004)
18. E A Kravchenko, Yu F Kargin, A V Egorysheva, Yu A Buslaev *Koord. Khim.* **27** 578 (2001) [c]
19. M H Cohen *Phys. Rev.* **96** 1278 (1954)
20. T P Das, A K Saha *Phys. Rev.* **98** 516 (1955)
21. P J Bryant, S Hacobian *Z. Naturforsch. A: Phys. Sci.* **41** 141 (1985)
22. B Aurivillius *Chem. Scr.* **24** 125 (1984)
23. M A Kennard, J Darriet, J Grannec, A Trassard *J. Solid State Chem.* **117** (1) 201 (1995)
24. E A Kravchenko, V G Orlov, V G Morgunov, Yu F Kargin, A V Egorysheva, M P Shlikov *Hyperfine Interact.* **158** 181 (2005)
25. V G Grebinnik, V N Duginov, V A Zhukov, B F Kirillov, E A Kravchenko, T N Mamedov, B A Nikol'skii, V G Ol'shevskii, V G Orlov, A V Pirogov, V Yu Pomyakushin, A N Ponomarev, V A Suetin *Yadernaya Fiz.* **56** (2) 71 (1993) [d]
26. V N Duginov, V G Grebinnik, T N Mamedov, V G Olshevsky, V Yu Pomjakushin, V A Zhukov, B F Kirillov, B A Nikolsky, V G Orlov, A V Pirogov, A N Ponomarev, V A Suetin, E A Kravchenko *Hyperfine Interact.* **85** 197 (1994)
27. V G Grebinnik, V N Duginov, V A Zhukov, E A Kravchenko, I A Krivosheev, T N Mamedov, B A Nikol'skii, V G Ol'shevskii, V G Orlov, V Yu Pomyakushin, A N Ponomarev, V A Suetin *Zh. Eksp. Teor. Fiz.* **108** 878 (1995) [e]
28. A I Kharkovskii, V I Nizhankovskii, E A Kravchenko, V G Orlov *Z. Naturforsch. A: Phys. Sci.* **51** 665 (1996)
29. V I Nizhankovskii, A I Kharkovskii, V G Orlov *Ferroelectrics* **279** 175 (2002)
30. R W Cochrane, R Harris, M J Zuckermann *Phys. Rep.* **48** 1 (1978)
31. V G Orlov, A A Bush, S A Ivanov, V V Zhurov *J. Low Temp. Phys.* **105** 1541 (1996)
32. V G Orlov, A A Bush, S A Ivanov, V V Zhurov *Fiz. Tv. Tela* **39** 865 (1997) [f]
33. A B Kuz'menko, E A Tishchenko, V G Orlov *J. Phys.: Condens. Matter* **8** 6199 (1996)
34. V N Denisov, A N Ivlev, A S Lipin, B N Mavrin, V G Orlov *J. Phys.: Condens. Matter* **9** 4967 (1997)
35. P W Selwood *Magnetochemistry* (New York: Interscience, 1956)
36. H A Harwig *Z. Anorg. Allg. Chem.* **444** 151 (1978)
37. L D Landau, E M Lifshits *Elektrodinamika Sploshnykh Sred* (Electrodynamics of Continuum) (Moscow: Nauka, 1982)
38. I E Dzyaloshinskii *Zh. Eksp. Teor. Fiz.* **37** 881 (1959) [e]
39. D N Astrov *Zh. Eksp. Teor. Fiz.* **38** 984 (1960) [e]
40. V J Folen, G T Rado, E W Stadler *Phys. Rev. Lett.* **6** 607 (1961)
41. H Schmid, in *Magnetoelectric Interaction Phenomena in Crystals* (Eds A J Freeman, H Schmid) (London: Gordon and Breach, 1975) p. 121
42. S L Hou, N Bloembergen *Phys. Rev.* **138** A1218 (1965)
43. A B Brik, I V Matyash, S S Ishchenko *Zh. Eksp. Teor. Fiz.* **79** 1902 (1980) [e]
44. C E Moore, in *Atomic Energy Levels* Vol. 1 (Washington, DC, 1949) Circular 468 N.B.S.
45. O K Andersen *Phys. Rev.* **12** B3060 (1975)
46. P Hohenberg, W Kohn *Phys. Rev. B* **136** 864 (1964)
47. V I Anisimov, J Zaanen, O K Andersen *Phys. Rev. B* **44** 943 (1991)
48. P W Anderson *Solid State Phys.* **14** 99 (1963)
49. K Blum *Density Matrix Theory and Applications* (New York, London: Plenum, 1981)

[a] — *Inorg. Mater. (Engl. Transl.)*
[b] — *Crystallogr. Rep. (Engl. Transl.)*
[c] — *Russ. J. Coord. Chem. (Engl. Transl.)*
[d] — *Phys. At. Nucl. (Engl. Transl.)*
[e] — *J. Exp. Theor. Phys. (Engl. Transl.)*
[f] — *Phys. Solid. State (Engl. Transl.)*